Lecture presented at International School of Electron Microscopy (Center for Scientific Culture) Erice, Trapani, Sicily, April 7-21, 1973

LBL-1472

INTRODUCTION TO CONTRAST ANALYSIS

Gareth Thomas

April 1973

Prepared for the U. S. Atomic Energy Commission under Contract W-7405-ENG-48

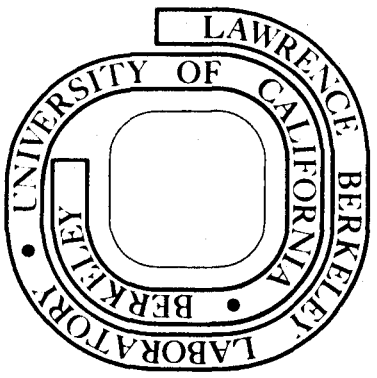

LBL-1472

DISCLAIMER

CHAPTER 2

INTRODUCTION TO CONTRAST ANALYSIS

Gareth Thomas

Professor of Metallurgy, Department of Materials Science and Engineering, College of Engineering; University of California, Berkeley, California

1. INTRODUCTION

In this chapter some simple geometrical approaches are discussed which may assist the beginning electron microscopist to better understand the nature of contrast and to facilitate the use of the microscope for characterizing the structure of materials. The bibliography listed at the end of Chapter 1 also applies to this chapter. In recent years developments have been made in what is now often referred to as "non-conventional" techniques such as weak beam dark field imaging (1) an example of which is shown in Fig. 1, and special effects from many beam interactions which become important at high energies. These phenomena are discussed elsewhere in this book, and in recent symposia (e.g., 2-6), but some mention of the latter will be made at the end of this chapter. Some important and useful applications of the effects of anomalous absorption which affect the symmetry properties of the image are also described.

The contrast in the image depends on the intensity distribution leaving the bottom surface of the specimen. Just as the diffraction pattern is the Fourier transform of the object, so is the image the Fourier transform of the diffraction pattern, so that all the points discussed in Chapter 1 apply directly to the understanding of contrast phenomena.

Although lattice imaging is a very powerful method with resolutions ~ 2Å (Fig. 2, Chapter 1), the more general technique of imaging is by amplitude contrast (i.e., without recombination of the phases of the transmitted and scattered waves) as is illustrated in Figs. 3, 4 (Chapter 1).

Amplitude contrast is achieved in either of two ways; a) formation of the bright field image by removing all diffracted beams or b) formation of the dark field image by allowing only one strong diffracted beam to form this image. These operations are carried out by means of the objective aperture which is inserted at the back focal plane of the objective lens (Fig. 3, Chapter 1). The dark field image is best obtained by gun tilting or by deflection so as to allow the beam to pass along the optic axis, thereby reducing errors from chromatic and spherical aberrations which occur if the objective aperture is moved off the optic axis (Figs. 3, 4, Chapter 1). An important point to realize is that for axial dark field the gun translation or beam deflection must be done such that the direction of $\bar{g}$ is reversed (i.e., if $\bar{g}$ is excited for bright field the corresponding gun tilt dark field should be obtained in $-\bar{g}$). This must be remembered when making the correct alignment between images and diffraction patterns.

2. KINEMATICAL APPROXIMATION-PERFECT CRYSTALS

As explained earlier the kinematical theory is applicable only to thin specimens and for conditions away from the exact Bragg position ($s \neq 0$). In Chapter 1 the kinematical intensities were derived, assuming all the energy is conserved (no absorption), viz.,

Diffracted $$|\psi|_D^2 \cong \left(\frac{F}{V}\right)^2 \frac{\sin^2 \pi ts}{(\pi s)^2} \quad (1)$$

Transmitted $$|\psi|_T^2 \cong 1 - \left(\frac{F}{V}\right)^2 \frac{\sin^2 \pi ts}{(\pi s)^2} \quad (2)$$

since $|\psi|_T^2 + |\psi|_D^2 = 1$, the kinematical theory predicts that bright and dark field images are complementary. In practice absorption occurs and this symmetry property is modified. However, the kinematical function predicts periodic variations of intensity with thickness for constant s (thickness fringes) or variations in intensity with s for constant thickness which lead to fringes about the Bragg contours. The (hkℓ) Bragg contour in the image corresponds to the hkℓ spot or kikuchi line in the diffraction pattern and is identified easily in dark field. Intensity minima occur in dark field whenever $s = n/t$ (constant t) or when $t = (n/s)$ for constant s. The periodic variation of $|\psi|^2$ with t leads to primary extinction $t_o = 1/s$, as discussed in Chapter I. In the dynamical theory (see the Chapter by Metherall), the extinction distance ξ_g is defined as $\pi V/\lambda F_g$ where V is the volume of the unit cell and F_g the structure factor for the particular reflection. The deviation from Bragg's condition is then often referred to by the dimensionless parameter $w = \xi_g s$ and in the kinematical case $w \gg 1$.

Every integral number of extinction distances all the electrons end up in the forward direction (transmitted) and in every odd half multiple extinction distances all electrons end up in the diffracted direction. The extinction distance is inversely proportional to the

scattering factor, which decreases with increasing scattering angle. Thus electrons have short extinction distances (100-1000Å), whereas x-rays have very long extinction distances.

The exchange of electron intensity between the transmitted and diffracted beams is exactly analogous to the motion of two coupled harmonic oscillators, which periodically exchange all the vibrational energy of the system. This forms the basis of the dynamical theory. The theory also shows that subsidiary maxima occur when $(s^2 + (\xi_g)^{-2})t^2 =$ integral. For thin crystals the value of t can be determined from measurements of s at subsidiary fringes either in the image or diffraction patterns (7), provided values of ξ_g are known.

From the foregoing we expect to produce contrast effects in an otherwise perfect crystal due to the following:

1) Changes in t - wedge fringes, fringes at inclined defects

2) Changes in s - Bragg contour fringes

3) Changes in orientation - changes s and g

Thus, e.g. in polycrystals the intensity varies from grain to grain because of differences in diffracting conditions. In general, therefore, contrast from crystals is not limited by resolution except in special cases. However, since the contrast is very orientation sensitive, it is essential to use a goniometric specimen holder preferably with as large a tilting range as possible so that the diffracting conditions can be varied in a systematic matter. Without such a stage, quantitative characterization of microstructure is almost impossible.

3. CONTRAST IN IMPERFECT CRYSTALS

a) General Comments

In practical materials we have to consider and characterize complicated microstructures including the following effects:

1. Changes in orientation with or without change in structure or composition e.g., grains, twins, precipitates.

2. Lattice defects, point defects, line defects, planar defects volume defects (effects due to elastic displacements)

3. Phase transformations a) changes in composition but not structure (e.g. spinodals) b) changes in composition and structure (general precipitation) c) changes in structure but not composition (e.g. martensites) d) Interphase interfaces (coherent, partially coherent, incoherent).

The contrast from these will arise from such effects as changes in the local diffracting conditions {changing s and g (d-spacings)}, phase changes on crossing interfaces, structure factor changes, changes in effective thickness (changing ξ_g). The situation can become quite complex especially when the defect density is high and strain fields overlap as in heavily deformed crystals, or crystals containing large volume fractions of particles.

The combination of bright and dark field imaging techniques and diffraction pattern analysis is essential in the characterization procedure. Analysis should always start from the diffraction pattern and most of the interpretation will be carried out at the microscope. For contrast work it is recommended that two-beam orientations be used

{as in Fig. 14(a) in Chapter 1}. For this reason it becomes essential to recognize orientations by inspection so that particular reflections of interest can be brought into operation. It is convenient to start by tilting the foil into a recognizable symmetry orientation and then tilting from there. The use of kikuchi maps greatly facilitates this process as will be shown later. Thus it cannot be emphasized too strongly how important it is to have a strong working knowledge of diffraction patterns and three dimensional crystallography. Thus all the informtaion developed in Chapter 1 is needed for analysis.

b) Information Requirements for Analysis (two beam conditions)

Generally we need to know the foil orientation, direction of diffraction vector, sign of s, and foil thickness.

1. Precise Orientation.

Because of the 180° ambiguity in spot patterns, the spot pattern by itself does not give the unique foil orientation and hence the geometry of defects in the foil are not known since the image is a two dimensional projection of the object. Thus the top of the foil is not distinguishable from the bottom, nor up from down. However a kikuchi pattern can be indexed uniquely (provided at least two poles are present) and this is facilitated by comparison to the appropriate kikuchi map. If kikuchi patterns are not obtainable then several methods can be utilized e.g. special absorption contrast effects such as the asymmetry in the dark field image when s is not quite zero. At $s > 0$ the bottom of the foil is in stronger contrast than the top; the reverse is true at $s < 0$. (e.g. See Fig. 15 and ref 8)

Alternatively, large angle tilting experiments observing the change in projected size of an object in the foil can be performed.

Once the orientation is known, the geometry of the foil is known and hence the sense of slope of planes and directions is known. This information is needed for quantitative analyses involving determining the sense of strain fields (e.g. vacancy or interstitial loops or faults).

Stereomicroscopy is useful also, because by this technique one can obtain information on the depth distribution of defects. Stereo pairs can be obtained by tilting 8-10° along a kikuchi band so that the diffracting conditions are not altered.

In orienting the pattern with the image, due to the inversion between the image and the diffraction pattern, rotate the diffraction pattern 180° (plus magnification rotation) with respect to the image, with the negatives both emulsion side up.* Crystallographic data can then be transferred directly from the pattern to the image. It is recommended that this be done directly on the negative (on the non-emulsion side) where it can be wiped off later after prints are made. In this way the geometry is preserved with minimum confusion, and the correct sense of the diffraction vector $\bar{g}$ in the image is retained. $\bar{g}$ is of course identified from the diffraction pattern and the region in the specimen corresponding to this g will reverse contrast in the dark field image of this reflection.

*This rotation is clockwise for Siemens Elmiskops, it is anticlockwise in the JEM 7. Thus it must be checked for each type of microscope.

Sign of s

The sign of the deviation parameter is important in several instances. In a two beam absorbing case the intensity in bright field is a maximum for $s > 0$ and in dark field at $s = 0$. These conditions are thus readily seen directly in the image. In the diffraction pattern for $s > 0$ the kikuchi line will lie to the outside of the corresponding spot since the reciprocal lattice point will be lying inside the reflecting sphere). For $s < 0$ the kikuchi lines lie inside the spot as e.g. in symmetrical orientations (Fig. 14(b) Chapter 1).

Foil Thickness

This can be found in several ways e.g. 1) trace analysis of projected defects that go completely through the foil (faults, twins, precipitates), 2) from measurements of subsidiary fringes either in the convergent beam pattern or from Bragg contour fringes (7). Recently a general method has been developed by Heimendahl (9) in which one or two latex balls of known diameter are applied to both foil surfaces in the area viewed. Changes in dimensions are observed after a known tilt and from the geometry the thickness can be calculated ~ 4% accuracy.

4. VISIBILITY OF LATTICE DEFECTS: GENERAL CRITERIA

Defects can be described in terms of translational vectors which represent displacements of atoms from their regular positions in the lattice. If the general displacement vector is $\vec{R}$, the kinematical amplitude scattered from the crystal as a whole becomes

$$\psi \sim \int_{\text{crystal}} [\exp 2\pi i(\vec{g} + \vec{s}) \cdot (\bar{r}_i + \vec{R})]dt \qquad (3)$$

or

$$\psi \sim \int_{\text{crystal}} [\exp 2\pi i\, \vec{s}\cdot\vec{r}_i \exp 2\pi i\, \vec{g}\cdot\vec{R}]dt \qquad (4)$$

since $g\cdot r_i$ = integer, and neglecting $\vec{s}\cdot\vec{R}_n$. (refer to Eq. 20, Chapter 1).

Thus the amplitude scattered by the perfect crystal is modified by the phase factor $2\pi\vec{g}\cdot\vec{R} = n2\pi$ and n can be integral, zero or fractional. The case $\vec{g}\cdot\vec{R} = 0$ is particularly important in contrast work. In has a simple physical meaning as can be seen from Fig. 7, Chapter 1. If $\vec{R}$ lies in the reflecting plane, d (and thus $|\vec{g}|$) is unaltered, so that the path difference between transmitted and diffracted waves is unaffected by $\vec{R}$. Since $\vec{g}$ is normal to (hkℓ), $\vec{g}\cdot\vec{R} = 0$, is the condition for no contrast due to a displacement $\vec{R}$ (Figs. 1, 2). It should be pointed out that $\vec{R}$ for a general defect varies with position. However for a stacking fault $\vec{R}$ is a constant equal to the displacement vector for the fault (section 8a). In this case no contrast arises when $\alpha = 2\pi\vec{g}\cdot\vec{R} = n\cdot 2\pi$, n integral.

The magnitude of $\vec{g}\cdot\vec{R}$ must be sufficient to change the intensity such that contrast is detectable over background (about 10% is enough). For example, for dislocation line defects in crystals $\vec{g}\cdot\vec{b} > \frac{1}{3}$ if the lines are to be detectable. Non-integral values of $\vec{g}\cdot\vec{b}$ for dislocations means that $\vec{b}$ is not a lattice translational vector and such dislocations must therefore always be associated with faults.

From a visibility viewpoint a general displacement $\vec{R}$ can be resolved along the principal axes

$$\vec{R} = \vec{R}_x + \vec{R}_y + \vec{R}_z$$

Examples of defects which are of general interest in the study of crystals and which can be described in terms of such displacements are: dislocations, dislocation loops, coherent volume defects e.g. point defect clusters, voids, coherent particles; planar defects such as stacking faults, domain boundaries (chemical, magnetic, electric, order), twin and grain boundaries, interphase interfaces etc.

The visibility of these defects can all be understood in terms of the simple $\vec{g}\cdot\vec{R}$ criterion. However the detailed interpretation of contrast behavior, such as the intensities, and variations in contrast with depth in the foil, behavior in the exact Bragg case, influence of other reflections, and the analysis of the sense of the displacements associated with the defects, require the application of the dynamical theory, as is described by Goringe.

A truly kinematical situation arises when large s values are used e.g. when imaging in g with ngs > 0 (n=2,3 or larger) excited. Such images are called weak beam images (because the intensity in g is low) and have high resolution (1). An example is shown in Fig. 1 which can be compared to Fig. 2.

From Eq. (5), $\vec{R}_z\cdot\vec{g}$ is always zero, hence only displacements lying in the plane of the foil are of importance in producing contrast. For screw dislocations the displacements R are always parallel to the Burgers vector $\vec{b}$ hence when $\vec{g}\cdot\vec{b} = 0$ screws are invisible. In the case of

an edge dislocation, the principal components of $\vec{R}$ are $\vec{b}$ and R_n (displacements normal to $\vec{b}$). For an edge dislocation with its half plane parallel to the beam, $\vec{g}\cdot\vec{b}$ = n(including 0), whereas $\vec{g}\cdot\vec{R}_n = 0$. On the other hand, if the dislocation is oriented with its half plane normal to the beam, $\vec{g}\cdot\vec{b} = 0$, but $\vec{g}\cdot\vec{R}_n$ = m(including zero). Thus because of the displacements $\vec{R}_n$ edge dislcoations do not necessarily go out of contrast completely when $\vec{g}\cdot\vec{b} = 0$, except under conditions when $\vec{g}\cdot\vec{R}_n$ also goes to zero. For this reason it is possible to see edge dislocations when their Burgers vectors are parallel to the incident beam. For example pure edge prismatic dislocation loops are visible (by so-called "residual contrast") when they are parallel to the foil plane as shown in Fig. 3. Notice in this case that loop segments are invisible where $\vec{g}\cdot\vec{R}_n = 0$ so the loops have a line of no contrast for those parts of the loop normal to $\vec{g}$. A similar contrast occurs for spherical strain fields such as in the case of coherent particles because the plane normal to g is unaffected by the strain, hence $\vec{g}\cdot\vec{R}_n = 0$; a well known example is Cu-Co, Fig. 4. In both cases therefore as the direction of $\vec{g}$ is changed so does the line of no contrast shift so as to always lie normal to g. This behavior allows such defects to be distinguished from perfect loops which also exhibit arced contrast (independent of g, $g\cdot b \neq 0$) when inclined to the foil plane (Fig. 9).

5. BURGERS VECTOR ANALYSIS

Table 1 gives examples of various $\vec{g}\cdot\vec{b}$ values for perfect dislocations in FCC, BCC and HCP structures, and tables 2, 3 gives $\vec{g}\cdot\vec{b}$ values for imperfect dislocations in fcc and hcp. By considering the various $\vec{g}\cdot\vec{b}$ possibilities it is possible to arrive at the most useful orientations needed for analysis (orientations [uvw] such that $[uvw]\cdot\vec{g} = 0$ Fig. 8, Chapter 1), and what changes in orientation are needed to arrive at the range of reflections required. These must lie within the range of the specimen tilting device. For this purpose the use of Kikuchi maps (10,11,13) greatly facilitates the required procedures. Several different reflections will normally be needed to obtain unique identifications. For partial dislocations $\vec{g}\cdot\vec{b} = \frac{1}{3}$ does not produce enough contrast to be detected so that this condition is one for invisibility (12).

As an illustration consider the case for hcp crystals for which Kikuchi maps are very helpful for several reasons (10,11) especially since the spot diffraction patterns from hcp crystals are in general less useful and much more difficult to analyze than those for cubic crystals. In addition to the complexities due to double diffraction (see Chapter 1), and that the c/a ratios differ from material to material, the d spacings of certain planes in hcp crystals are so close together that obtaining two beam orientations, e.g., in $\langle 11\bar{2}0 \rangle$ foils and unambiguously identifying the foil orientation, may be impossible, in certain cases. The above problems can be circumvented if foils thick enough to produce Kikuchi reflections are used. In general, Kikuchi patterns become increasingly useful as the symmetry

Table 1. Values of $\bar{g}\cdot\bar{b}$ for Perfect Dislocations

a) FCC

Plane of Dislocation	b / g	$\bar{g}\cdot\bar{b}$		
		$1\bar{1}1$	$\bar{1}11$	$11\bar{1}$
$1\bar{1}1$ or $1\bar{1}\bar{1}$	1/2 [110]	0	0	1
$1\bar{1}\bar{1}$ or $11\bar{1}$	1/2 [101]	1	0	0
$1\bar{1}1$ or $11\bar{1}$	1/2 [011]	0	1	0
111 or $11\bar{1}$	1/2 [$1\bar{1}0$]	1	$\bar{1}$	0
111 or $1\bar{1}1$	1/2 [$10\bar{1}$]	0	$\bar{1}$	1
111 or $\bar{1}11$	1/2 [$0\bar{1}1$]	1	0	$\bar{1}$

b) BCC

Plane of Dislocation	b / g	$\bar{g}\cdot\bar{b}$		
		$0\bar{1}1$	$1\bar{1}0$	110
$0\bar{1}1$,$1\bar{1}0$,$\bar{1}01$	1/2 111	0	0	1
$0\bar{1}1$,110,101	1/2 $\bar{1}11$	0	$\bar{1}$	0
$\bar{1}01$,110,011	1/2 $1\bar{1}1$	1	$\bar{1}$	0
101,$\bar{1}10$,011	1/2 $\bar{1}\bar{1}1$	1	0	$\bar{1}$

c) HCP

Perfect dislocations in the hcp lattice are a/3 ⟨ $2\bar{1}\bar{1}0$ ⟩ (three in number), a[0001] (one in number) and a/3 ⟨ $11\bar{2}3$ ⟩ (six in number).

The table below illustrates for orientation near [$1\bar{1}05$] the $\bar{g}\cdot\bar{b}$ conditions necessary to distinguish dislocations invisible in g = $1\bar{1}00$

c) HCP

b / g	$\bar{g}\cdot\bar{b}$		
	$2\bar{2}00$	$\bar{2}3\bar{1}1$	$\bar{3}211$
1/3 [$\bar{1}\bar{1}20$]	0	-1	1
1/3 [$\bar{1}\bar{1}23$]	0	0	2
1/3 [$11\bar{2}3$]	0	2	0

3211

Table 2. Values for g·b for Imperfect Dislocations in the FCC Lattice[a]

Fault Plane	b	200	$0\bar{2}0$	$2\bar{2}0$	220	111	$1\bar{1}\bar{1}$	$4\bar{2}\bar{2}$	311
(111)	$a/6[\bar{1}\bar{1}2]$	-1/3	1/3	0	-2/3	0	-1/3	-1	-1/3
	$a/6[2\bar{1}\bar{1}]$	2/3	1/3	1	1/3	0	2/3	2	2/3
	$a/6[\bar{1}2\bar{1}]$	-1/3	-2/3	-1	1/3	0	-1/3	-1	-1/3
$(11\bar{1})$	$a/6[2\bar{1}1]$	2/3	1/3	1	1/3	1/3	1/3	4/3	1
	$a/6[\bar{1}\bar{1}\bar{2}]$	-1/3	1/3	0	-2/3	-2/3	1/3	1/3	-1
	$a/6[\bar{1}21]$	-1/3	-2/3	-1/3	1/3	1/3	-2/3	-5/3	0
$(1\bar{1}1)$	$a/6[\bar{1}2\bar{1}]$	-1/3	2/3	1/3	-1	-2/3	1/3	1/3	-1
	$a/6[\bar{1}12]$	-1/3	-1/3	-2/3	0	1/3	-2/3	-5/3	0
	$a/6[21\bar{1}]$	2/3	-1/3	1/3	1	1/3	0	4/3	1
$(\bar{1}11)$	$a/6[\bar{2}\bar{1}\bar{1}]$	-2/3	1/3	-1/3	-1	-2/3	0	-2/3	-4/3
	$a/6[1\bar{1}2]$	1/3	1/3	2/3	0	1/3	0	1/3	2/3
	$a/6[12\bar{1}]$	1/3	-2/3	-1/3	1	1/3	0	1/3	2/3
(111)	a/3[111]	2/3	-2/3	0	4/3	1	-1/3	0	5/3
$(11\bar{1})$	$a/3[11\bar{1}]$	2/3	-2/3	0	4/3	1/3	-1/3	4/3	1
$(1\bar{1}1)$	$a/3[1\bar{1}1]$	2/3	2/3	4/3	0	1/3	1/3	4/3	1
$(\bar{1}11)$	$a/3[\bar{1}11]$	-2/3	-2/3	-4/3	0	1/3	-1	-8/3	-1/3
(111)	$a/6[1\bar{1}0]$	1/3	1/3	2/3	0	0	1/3	1	1/3
	$a/6[01\bar{1}]$	0	-1/3	-1/3	1/3	0	0	0	0
	$a/6[10\bar{1}]$	1/3	0	1/3	1/3	0	1/3	1	1/3
$(1\bar{1}1)$	$a/6[\bar{1}01]$	-1/3	0	-1/3	-1/3	0	1/3	-1	1/3
	a/6[110]	1/3	-1/3	0	2/3	1/3	0	1/3	2/3
	a/6[011]	0	-1/3	-1/3	1/3	1/3	-1/3	-2/3	1/3
$(11\bar{1})$	a/6[101]	1/3	0	1/3	1/3	1/3	0	1/3	2/3
	$a/6[1\bar{1}0]$	1/3	1/3	2/3	0	0	1/3	1	1/3
	a/6[011]	0	-1/3	-1/3	1/3	1/3	-1/3	-2/3	1/3
$(\bar{1}11)$	a/6[110]	1/3	-1/3	0	2/3	1/3	0	1/3	2/3
	$a/6[0\bar{1}1]$	0	1/3	1/3	-1/3	0	0	0	0
	a/6[101]	1/3	0	1/3	1/3	1/3	0	1/3	2/3

[a] $a/6\langle 112\rangle$ are Shockley partials; $a/3\langle 111\rangle$ are Frank partials; and $a/6\langle 110\rangle$ are stair rod dislocations.

of the crystal system decreases, and for recognizing orientations under two-beam conditions. Furthermore, for hcp structures, the basal-plane orientation and orientations within about a 20-deg tilt from [0001] are all that are required for solving problems such as Burgers vector determinations. This tilting range is within the range available for most commercial tilting stages.

(a) Perfect Dislocations

Perfect dislocations must vanish for one of the $20\bar{2}0$ Kikuchi bands. These, rather than $10\bar{1}0$ are used because of their higher intensities. If we designate the particular reflection to be the $2\bar{2}00$, then b must be one of the following: $\pm \frac{1}{3}[\bar{1}\bar{1}20]$, $\pm \frac{1}{3}[\bar{1}\bar{1}23]$, or $\pm \frac{1}{3}[11\bar{2}3]$. Since a dislocation image vanishes for any Kikuchi band which converges to the pole of the Burgers vector, ($\bar{g}\cdot\bar{b} = 0$) any two Kikuchi bands converging to the $[\bar{1}\bar{1}23]$ and $[11\bar{2}3]$ poles can be used to distinguish between the three possibilities. Reference to the Kikuchi map [Fig. 25, Chapter 1] shows that the nearest of such bands are the $\bar{2}3\bar{1}1$ and $\bar{3}211$ which intersect at the $[1\bar{1}05]$ pole. This pole can be reached by a direct tilt along the $11\bar{2}0$ Kikuchi band (e.g., for Ti this involves about a 14° tilt.) Table 1c shows the $\bar{g}\cdot\bar{b}$ values for the three reflections used in the procedure, and clearly shows that they are sufficient to determine the Burgers vector.

(b) Imperfect Dislocations

Imperfect dislocations must vanish for one of the $11\bar{2}0$ Kikuchi bands. If we designate the reflection to be the $2\bar{1}\bar{1}0$, then b must be one of the following: $\pm \frac{1}{3}[0\bar{1}10]$, $\pm \frac{1}{6}[0\bar{2}23]$, or $\pm \frac{1}{6}[0\bar{2}23]$. Table 3(a)

Table 3(a). Values of $\mathbf{g}\cdot\mathbf{b}$ for imperfect dislocations, [0001] orientation.

	b		
g	$\frac{1}{3}[0\bar{1}10]$	$\frac{1}{6}[0\bar{2}23]$	$\frac{1}{6}[02\bar{2}3]$
$20\bar{2}0$	$\frac{2}{3}$	$-\frac{2}{3}$	$\frac{2}{3}$
$2\bar{2}00$	$\frac{2}{3}$	$\frac{2}{3}$	$-\frac{2}{3}$
$02\bar{2}0$	$-\frac{4}{3}$	$-\frac{4}{3}$	$\frac{4}{3}$
$2\bar{1}\bar{1}0$	0	0	0
$\bar{1}2\bar{1}0$	-1	-1	1
$\bar{1}\bar{1}20$	1	1	-1

Table 3(b). Values of $\mathbf{g}\cdot\mathbf{b}$ for partial dislocations using $[0001]-[4\bar{2}\bar{2}9]$ orientations.

	b		
g	$\frac{1}{3}[0\bar{1}10]$	$\frac{1}{6}[0\bar{2}23]$	$\frac{1}{6}[02\bar{2}3]$
$2\bar{1}\bar{1}0$	0	0	0
$\bar{3}032$	1	2	0
$\bar{3}302$	-1	0	2

Table 3(c). Values of $\bar{\mathbf{g}}\cdot\bar{\mathbf{b}}$ for partial dislocations using $[0001]-[1\bar{1}03]$ orientations.

	b		
g	$\frac{1}{3}[0\bar{1}10]$	$\frac{1}{6}[0\bar{2}23]$	$\frac{1}{6}[02\bar{2}3]$
$2\bar{1}\bar{1}0$	0	0	0
$\bar{2}111$	0	$\frac{1}{2}$	$-\frac{1}{2}$
$\bar{3}302$	-1	0	2

shows that other $11\bar{2}0$ and $20\bar{2}0$ reflections cannot be used to distinguish between the three possibilities. In this case the poles of interest are the $[0\bar{2}23]$ and $[02\bar{2}3]$, and the corresponding Kikuchi bands are the $\bar{3}302$ and $\bar{3}032$ which intersect at the $[4\bar{2}\bar{2}9]$ pole. This pole can be reached by tilting (~ 24 deg for Ti) along the $01\bar{1}0$ Kikuchi band. Table 3b shows the $\bar{g}\cdot\bar{b}$ values for the three reflections used in the procedure.

Since the tilt (~ 24 deg) needed to reach the $[4\bar{2}\bar{2}9]$ pole from the [0001] orientation is very near the limit of many specimen tilting devices, an alternate procedure involving somewhat smaller tilts can be used by utilizing the $\bar{2}111$ forbidden reflections resulting from double diffraction. The procedure is the same as the one described above except that the foil is tilted into the $[1\bar{1}03]$ rather than the $[4\bar{2}\bar{2}9]$ orientation. (For Ti this involves about a 20 deg tilt.) Remembering that extinction of imperfect dislocations occurs when $|\bar{g}\cdot\bar{b}| \leq \frac{1}{3}$, Table 3c shows that the $\bar{2}111$ and $\bar{3}302$ reflections accessible in the $[1\bar{1}03]$ orientation provide sufficient information for a unique determination of the Burgers vector.

In many problems, the object is to distinguish between dislocations having Burgers vectors of the same type. For example, one may wish to distinguish between dislocations of the primary and secondary slip systems having Burgers vectors of the form $\frac{1}{3}\langle 2\bar{1}\bar{1}0\rangle$. The lowest-order reflections needed for $g\cdot b = 0$ conditions are of the form $10\bar{1}0$ and $\bar{2}201$. $10\bar{1}0$ reflections cannot distinguish between $\frac{1}{3}\langle 2\bar{1}\bar{1}0\rangle$ and $\frac{1}{3}\langle 2\bar{1}\bar{1}3\rangle$. Furthermore, the tilting device often tilts further in one direction than in another. If the [0001] orientation does not lie within the

range of the tilt, then all three $10\bar{1}0$ Kikuchi bands may not be accessible. On the other hand, the $\bar{2}201$ Kikuchi bands intersect in such a way as to form six equivalent triangles situated symmetrically about the [0001] zone axis. The six triangles are centered on the $\langle 1\bar{1}03 \rangle$ poles and have vertices composed of poles of the form $\langle 1\bar{2}16 \rangle$ and $\langle 0\bar{1}12 \rangle$. Any one of the six triangles can be used to distinguish between the three $\frac{1}{3}\langle 2\bar{1}\bar{1}0 \rangle$ Burgers vectors. For example, if the foil is initially in some high-index orientation such as the $[0\bar{3}34]$, the [0001] zone axis may lie outside the range of the specimen tilting device. In this case, the triangle centered on the $[0\bar{1}13]$ pole can be used where $\bar{2}201$, $02\bar{2}1$, and $20\bar{2}1$ Kikuchi bands are readily accessible. An example of this application is shown in Fig. 5 for dislocations in Ag_2Al (I4). The dislocations occur in the form of perfect loops clustered in slip bands lying parallel to the trace of the primary slip plane. Figure 5(a)-(c) is a series of micrographs of a typical slip band. The corresponding reflections are indicated on the Kikuchi map, Fig. 5(d). The micrographs have been oriented with respect to the Kikuchi map so that the slip band lies parallel to the trace of the $(01\bar{1}0)$ plane, i.e., parallel to the $01\bar{1}0$ Kikuchi band. As shown in section 7(b), in fcc metals the Burgers vector of double arc loops can be uniquely determined from the direction of the line-of-no-contrast (18); however, in hcp metals the line-of-no-contrast can only be used to eliminate all but three of the nine possible Burgers vectors of the form $\frac{1}{3}\langle 2\bar{1}\bar{1}0 \rangle$ and $\frac{1}{3}\langle 2113 \rangle$. As indicated in Fig. 5(a), the line-of-no-contrast is parallel to the $[1\bar{1}00]$ direction; hence, the double-arc loops can have any of the following Burgers vectors: $\pm \frac{1}{3}[\bar{1}\bar{1}20]$,

$\pm \frac{1}{3}[\bar{1}\bar{1}23]$, or $\pm \frac{1}{3}[1123]$. In order to distinguish between these, the foil was tilted to the nearest $\bar{2}201$-triangle centered on the $[0\bar{1}13]$ pole. Figure 5(a) was taken with $2\bar{1}\bar{1}0$ so that all three possible types of dislocations can be in contrast. Figure 5(b) shows all loops are out of contrast with $\bar{2}201$; therefore, they all have the identical Burgers vector $\frac{1}{3}[\bar{1}\bar{1}20]$. By tilting to $g = 02\bar{2}1$, the pileup of dislocations within the band and the helical dislocations near the edges vanish [Fig. 5(c)]. Therefore, these dislcoations have the Burgers vector $\frac{1}{3}[2\bar{1}\bar{1}0]$.

6. MAGNITUDE OF $g \cdot b$

For hcp crystals, $g \cdot b$ can be 2 in low order reflections for perfect dislocations (Table 1c). In these conditions the image is then doubled. This effect is useful for distinguishing different Burgers vectors. $g \cdot b > 1$ is not commonly observed in fcc or bcc crystals unless high order reflections are obtained. For example in the $[\bar{1}10]$ fcc orientation a screw dislocation with $b = a/2\ [110]$ would show a double image in $g = 220$, a single image in $g = 111$ and be invisible in $g = 002$. Thus in principle studies of the image in different reflections enable the magnitude of $\bar{b}$ as well as its direction to be determined.

For partial dislocations some complexities arise, due to dynamical effects. In the fcc structure especially when anisotropy is considered (16) it has been shown that whereas $g \cdot b = \pm \frac{1}{3}$ is always an invisibility criterion, the case for $g \cdot b = \mp \frac{2}{3}$ leads to visibility or invisibility depending on the sign of s and the position in the foil (thickness dependence). These difficulties have been discussed by Clarebrough (15)

who suggests that computations will be necessary to determine Burgers vectors of partials. This approach is facilitated by using image simulation techniques for direct comparisons of computed data with experimental results (16).

7. IMAGE POSITION

The position of the dislocation image with respect to the actual line depends on the sign of s. This can be seen geometrically by considering Fig. 6. In (a) we set $s > 0$ and assume an edge dislocation is oriented as shown. We see that if $\vec{g}$ points to the right the sense of tilt of the planes on the LHS causes greater deviation $s \gg 0$ from diffraction whereas on the RHS the reverse is true. In this case the image will thus appear to the RHS. Simularly in (b) if the foil is tilted slightly to make s negative, the image flips to the LHS. Thus on crossing an extinction contour (s changing sign) the image changes position. The same effect is true when g is changed sign (for s invariant).

Thus without pre-defining the sense of the Burgers vector as long as the sign of s and the direction of $\vec{g}$ are known it is possible to reconstruct in the foil the orientation of the dislocation which gives rise to the observed image shift when g or s changes sign. This result has useful applications.

(a). Dislocation pairs

Dislocation pairs are of two types, viz. the dipole (two dislocations of opposite sign) and the superdislocation (two of the same sign). These can be distinguished by the manner in which the images change

with changing g or s as is seen in Fig. 7(a). The example of Figs. 7b,c for austenitic stainless steel obtained by changing the sign of $\bar{g}$ shows that the pairs at A are superdislocations, indicating the existence of order. These experiments are particularly valuable for studying order in alloys of similar elements for which possible superlattice reflections cannot be detected in the electron diffraction patterns, e.g., brass (Cu-Zn) and Fe-Cr-Ni alloys (17). Pairs can be distinguished from double images since the latter occur only when more than one strong reflection operates on opposite sides of a single dislocation, or when $\bar{g}\cdot\bar{b} = 2$.

(b) Loops

The fact that the dislocation image changes position with change in sign of g or s can be used to determine whether dipoles or loops are vacancy or interstitial in character, again without prior definition of the sign of $\vec{b}$.

Figure 8 illustrates how the images vary with change in sign of g or s. If the defect lies along the plane inclined from bottom left to top right the vacancy loop will always be in outside contrast for $\vec{g}$ to the RHS and $s > 0$.

It is important to notice that if the defects in Fig. 8 were inclined in opposite sense (top left to bottom right), then the vacancy will be in outside contrast at $s > 0$ with $\vec{g}$ to the LHS. Figure 9 shows an actual example for this case, for loops in quenched aluminum. Thus it is essential to know the sense of inclination of the defect and to correctly orient the direction of g on the micrograph as was discussed earlier in this chapter. The example of Fig. 9 also shows that for

perfect loops the Burgers vector is perpendicular to the line of no contrast dividing the loop image into arcs (18). For fcc crystals this line is a ⟨110⟩ and so $\bar{b}$ can be uniquely found once the foil is correctly oriented. This double-arc contrast arises because the strain fields tend to cancel at the strong edge components of the loops. For two beam imaging conditions at $s \sim 0$ this rule appears to hold generally for large perfect loops in fcc, bcc and hcp crystals, and is thus quite useful when large numbers of defects are to be analysed (19).

8. PLANAR DEFECTS

(a) Stacking Faults

For purposes of illustration consider stacking faults in the FCC structure. Two possibilities exist, viz. formation of a stacking fault by the splitting of a whole dislocation under a shear stress:

$$a/2[\bar{1}01] = a/6[\bar{1}\bar{1}2] + a/6[\bar{2}11] \quad \text{on (111)}$$

or the creation of a fault by growth or point defect aggregation forming imperfect edge prismatic loop dislocations of the a/3⟨111⟩ type.

The stacking fault is the least complicated of planar defects since only a displacement of the crystal across the fault plane is involved (i.e., no change in s or g). The contrast was first considered by Whelan and Hirsch (20). A wave crossing a faulted region of a crystal suffers a phase change $\alpha = 2\pi\vec{g}\cdot\vec{R}$, and similar to the wedge case, fringes occur when the fault is inclined in the foil. If $\vec{R}$ is a lattice translation vector, then the phase contrast is zero since $\vec{g}\cdot\vec{R}$ is integral. For stacking faults, however, $\vec{R}$ cannot be a lattice translation vector, but particular values can occur for which $\vec{g}\cdot\vec{R}$ is integral. This result

affords a means for studying the faults in a similar manner to that adopted for dislocations, putting $\vec{R}$ equal to the fault vector.

In FCC materials $\vec{R}$ = a/6 ⟨112⟩ or a/3 ⟨111⟩. Therefore α can take the values $\alpha = \frac{2\pi(h + k + 2\ell)}{6}$ or $\frac{2\pi}{3}(h + k + \ell)$. In either case $\alpha = \pm 2\pi/3$, (fault visible), or $n2\pi$, (fault invisible) hence the shear a/6 ⟨112⟩ fault cannot be distinguished from the a/3 ⟨111⟩ fault purely from fringe contrast, as expected since physically they are identical.

The possible $\vec{g}\cdot\vec{R}$ values for faults in fcc or dc crystals can be found from Table 2. The values of $\alpha = 2\pi\vec{g}\cdot\vec{R}$ change along each parallel <111> row of the reciprocal lattice (See Fig. 16a, Chapter 1). Thus faults are visible in reflections along the 2nd, 3rd, 5th, 6th etc <111> rows; but invisible in the 1st, 4th,....etc.

We will now consider various examples of contrast to be expected from faults bounded by partials. Consider the (111) fault plane with the operating partials a/6[1$\bar{2}$1] and a/6[2$\bar{1}\bar{1}$]. It is assumed also that $g\cdot b = \pm \frac{2}{3}$ will always be visible (remembering that this is not necessarily true in all situations.

1) $\vec{g}$ = [200]

a/2[1$\bar{1}$0] = a/6[1$\bar{2}$1] + a/6[2$\bar{1}\bar{1}$] on (111)

g·b 1 + 1/3 + 2/3

α for fault = $2\pi/3$ fault visible and one partial visible

2) g = [200]

a/2[01$\bar{1}$] = a/6[$\bar{1}$2$\bar{1}$] + a/6[11$\bar{2}$] on (111)

g·b 0 - 1/3 + 1/3

α for fault = $-2\pi/3$ fault visible but no partials visible

3) $g = [2\bar{2}0]$

$a/2[01\bar{1}] = a/6[\bar{1}2\bar{1}] + a/6[11\bar{2}]$ on (111)

$g \cdot b$ -1 -1 0

α for fault = 0; fault invisible, only one partial visible.

This case could be mistaken for a perfect dislocation.

These cases are illustrated by the sketches in Fig. 10. Figure 11 shows an example of Case 1 in which faults of opposite sense are present at A and B.

If one wishes to distinguish between a 1/3(111) and a 1/6(112) fault it is necessary to determine the Burgers vector of the bounding dislocations. Reference to Table 2 for FCC crystals shows the reflections needed to make this distinction. For a fault on a {111} use of $g = \langle 2\bar{2}0 \rangle$ and $g = \langle 200 \rangle$ is sufficient and a foil in $\langle 001 \rangle$ will be required e.g., Fig. 12; the partial at A on $(1\bar{1}\bar{1})$ must be the Shockley, $\vec{b} = a/6[12\bar{1}]$

(b) Determination of Type of Stacking Fault

The dynamical theory predicts the dependence of the intensity of the fringes on the sign of α. In bright field for α positive the first fringe is light whereas for α negative the first fringe is dark. The reverse is true for dark field images although the effect of absorption modifies the symmetry such that the fringes are complementary only at the lower surface of the foil (Fig. 13). This dependence of the colour of the first fringe on α can also be obtained intuitively by considering phase advance or retardation on an amplitude phase diagram.

The above rules can be used to determine whether a fault or thin slab of precipitate is intrinsic or extrinsic (21,22), but it is essential to know the sense of slope of the fault plane with respect to $\bar{g}$. Since we can consider an extrinsic fault as one due to the insertion of an extra plane of atoms and an intrinsic fault as one formed by removal of a plane, the sign of $\vec{R}$ will be opposite for an extrinsic and intrinsic fault and hence the sign of $\alpha = 2\pi\vec{g}\cdot\vec{R}$ will be reversed for these cases when the same $\vec{g}$ operates. We now define the two types of faults as follows. Consider the top half of the crystal at rest and the bottom half is now displaced by the fault displacement vector (Fig. 14). The sense of the displacements are shown. Now knowing the direction of $\vec{g}$, after allowing for optical rotations, and observing the color of the first fringe, we can identify whether β is acute or obtuse and hence determine the nature of the fault. For example in the FCC case the value of $\alpha = 2\pi|g||R| \cos\beta = \pm 2\pi/3$, where $|\vec{R}| = a\sqrt{3}/3$, then suppose $g = 200$ and is to the R.H.S. of the fault. $\beta = \pm 1\sqrt{3}$, since $\vec{R} = \pm a/3[111]$. If the first fringe is white, α is positive, i.e. $\alpha = 4\pi/3(\sqrt{3}) \cos\beta = 2\pi/3$ if $\cos\beta = -1\sqrt{3}$. That is β must be obtuse and the fault must be intrinsic. For the same situation an extrinsic fault would show a black first fringe. These rules are summarized in Table 4 for faults oriented as shown in Fig. 14. In practice the micrograph can always be oriented such that the fault plane slopes as shown in these sketches.

Figure 15 shows an example of the use of these rules, and illustrates how rapidly one can analyse the fault inclination by dark field imaging at $s \neq 0$. The first fringe is thus the most intense fringe when $s < 0$

Table 4. Determination of Nature of Stacking Faults in FCC Crystals[a]

$\vec{g}$	Orientation of $\vec{g}$	Color of First Fringe *	
		Bright	Dark
200	L	E	I
	R	I	E
400	L	I	E
	R	E	I
220	L	I	E
	R	E	I
111	L	I	E
	R	E	I

[a] Ref. 22 * Bright Field

slight deviation in dark field.

The reader can show that in Fig. 12 the faults on $(1\bar{1}\bar{1})$ and (111) slope in opposite sense and since the first fringe is bright in both cases they must be extrinsic and intrinsic respectively.

(c) Overlapping Faults

Consider two overlapping faults of the same kind (Fig. 16a). If these are close together the phase factors add giving a net phase shift of $2\pi/3 + 2\pi/3 = -2\pi/3$, i.e. the color of the first fringe changes at the point of overlap. If three faults overlap the phase change is 2π = zero and no contrast occurs. If the faults are far apart the outer fringes will be of the same color (Fig. 16b).

Similarly if two overlapping intrinsic-extrinsic faults exist, if they are close together $\alpha = +2\pi/3 + (-2\pi/3) = 0$ and no contrast occurs. However if they are far enough apart the outer fringes will be of opposite color and the center part of the overlap will have weak or zero contrast where the two phase shifts cancel (Fig. 16(c)).

(d) Ordered Alloys: Antiphase Boundaries

A fault in the periodic array of ordered planes of atoms gives rise to an antiphase boundary. If the displacement of the crystal associated with this type of fault is $\vec{R}$ = [uvw] then the phase shift $\alpha = 2\pi\vec{g}\cdot\vec{R} = 2\pi(hu + kv + \ell w)$. Ordered alloys are often characterized by having primitive symmetry in that all values of $hk\ell$ are allowed. The superlattice reflections are those that would not exist in the disordered alloy, e.g. in the B2 superlattice, based on a body centered structure (CsCl):

$$F = f_A + f_B \quad h + k + \ell \text{ even} \quad \text{(fundamental)}$$
$$= f_A - f_B \quad h + k + \ell \text{ odd} \quad \text{(superlattice)}$$

In this superlattice $\vec{R} = a/2\langle 111 \rangle$ hence

$$\alpha = \pi(h + k + \ell) = 0 \quad \text{for } h + k + \ell \text{ even}$$
$$= \pm\pi \quad \text{for } h + k + \ell \text{ odd}$$

in other words, only superlattice reflections (e.g. 100, 111) can produce phase contrast in this case. This follows because $a/2\langle 111 \rangle$ is a $\vec{T}$ vector for the disordered alloy. In the case of π boundaries the first fringe is always dark in bright field.

Another type of superlattice is the Ll_2 superlattice based on a face-centered structure. In this case

$$F = 3f_A + f_B \quad \text{for} \quad hk\ell \text{ unmixed}$$
$$f_A - f_B \quad \text{for} \quad hk\ell \text{ mixed}$$

One type of antiphase boundary vector $\vec{R}$ is $a/2\langle 110 \rangle$, hence $\alpha = \pi(h + k)$. Thus for fundamental reflections α is always zero ($a/2\langle \bar{1}10 \rangle$ is a $\vec{T}$ vector for the disordered alloy) and is zero or $\pm\pi$ for superlattice reflections.* Again in bright field the first fringe is always black. Another possible antiphase vector is $a/6\langle 112 \rangle$ -- a partial vector in the disordered alloy. Hence for fundamental reflections $\alpha = 0$ or $\pm 2\pi 3$ as for a stacking fault. In the case of superlattice reflections α can be $\pm\pi/3$, $\pm 2\pi/3$, $\pm\pi$ or 0. If α is $+\pi/3$ the contrast will be the same

*In Fig. 21 a,b,c chapter 1 faint APB contrast is visible in the fundamental reflection-this is because there is a faint contribution from the superlattice reflection (e.g. if the fundamental is 2g, g is also excited to some extent e.g. Fig. 2d).

as that for $\alpha = -2\pi/3$ and vice versa for $\alpha = -\pi/3$. Examples are given in my later chapter in Figs. 7, 11, 12, of part 2.

The periodicity of fringes for superlattices is quite different from that of stacking faults in non-ordered materials due to the fact that the extinction distances for superlattice reflections are much greater than those for fundamental reflections. Few fringes are therefore visible in the case of domain boundaries.

9. ADDITIONAL EFFECTS

Other factors can give rise to contrast due to planar defects. So far we have considered phase contrast due to a displacement without change in orientation or structure. This is exactly true for stacking faults in fcc crystals, but e.g. is not generally true for planar defects, or for crystals of lower symmetry. For example the value of both s and g can change across a fault giving rise to Moiré (Δg) and other fringes, sometimes called δ fringes, discussed in detail elsewhere in this book by Amelinckx (see also ref. 23). Figure 9. part 2 of my later chapter shows an example of δ fringes at antiferromagnetic domain walls. An example of Moiré fringes across coherent interfaces in Cu-Mn-Al has been given in Fig. 15 Chapter 1. Measurements of fringe spacings enable the mismatch across the interface to be calculated especially for very small mismatches (Δg small, D(fringe spacing)large). Imaging at conditions when $s \gg 0$ e.g. dark field weak beam is also useful for distinguishing Moiré contrast from interface dislocations as has been shown for coarsened spinodal alloys by Bouchard et.al (25).

The analysis of contrast changes across interfaces is necessary if the nature of the interface is to be determined. Recently, considerable interest has being generated in grain boundaries and interphase interfaces (see e.g. refs. 24, 25).

10. SMALL VOLUME DEFECTS-PRECIPITATES

For coherent defects the contrast can be considered by use of the appropriate displacements (Eq. 5) in the intensity calculations. The visibility criterion $\vec{g}\cdot\vec{R}$ enables the direction of $\vec{R}$ to be established and no difficulties arise in the case of plates, rods, and spheres. (See ref 26 for review) Contributing to contrast in the case of precipitates will be intensity changes due to the differences in structure factor between precipitate and matrix. Figure 17(a) shows diffraction contrast from small {100} coherent plates in a [011] foil of Al-4%Cu. These plates have strain fields normal to the {001} habit plane so $\vec{R} = \langle 001 \rangle$. In Fig. 17a, since $\vec{g} = 200$, only plates on (100) are visible ($\vec{g}\cdot\langle 100 \rangle$ criteria); in (b) which is a dark field image of the [100] streak from θ" occurring in the diffraction pattern (c), "structure factor" contrast is obtained for the (100) plates. In Fig. 17d which is a superb example of the powerful technique of lattice imaging, small G. P. zones of thickness ~ 8Å and diameter 110Å are actually resolved. In Fig. 17(d) the strains from each G. P. zone can be measured directly from the displacements of the (002) planes along the lines marked a, b, c, d. The strains fall off to near zero at about 30Å from the zone center.

This technique is very valuable for analysing the complex situation existing when there is a very large density of defects (e.g. G. P. zones in Al-4%Cu can exist in densities $\geqslant 10^{19}$ per cm^3) such that strain fields overlap. The resultant strain patterns in amplitude-contrast images are very complex and in many cases completely mask the individual particles. Such contrast is referred to as tweed or basket-weave and often occurs in ⟨ 110 ⟩ in many alloys undergoing different types of phase transformations (26). Progress is being made in understanding these images by computational techniques (27) and lattice imaging (28, 29).

Analysis is also difficult when large densities of small defect clusters are produced by irradiation (see Chapter by Wilkens). The contrast is very depth dependent, which makes identification in terms of vacancy or interstitial character rather tedious. These difficulties have been discussed in detail recently (30) and it is clear that computer simulation and image processing techniques will also be essential for these problems (31).

13. MANY BEAM EFFECTS AND CONTRAST AT HIGH VOLTAGES

At high voltages the sphere of reflection becomes much flatter (Table 1, Chapter 1) so that many beams are excited. Furthermore the electron scattering factors increase with voltage due to the increase of the relativistic mass (Fig. 5, Chapter 1) so that the diffracted intensities are higher. These factors mean that two beam theory no longer applies and it is more difficult or impossible to predict contrast from simple geometrical arguments.

However if many beam theory is used it appears that useful practical applications become possible. A particularly interesting effect is that of critical voltage where intensities of second order reflections go through a minimum at certain voltages (e.g. 430 kV for 222 in Al) see e.g. ref. 4. Since this phenomenon will be discussed elsewhere in this book, here we indicate two general examples of many beam effects.

(a) Dislocation Contrast

Some results of up to 12 beam dynamical contrast calculations for systematic orientations[2,3,32,33] have indicated that high order reflections at high voltages may provide improved dislocation resolution.* For example the bright field images of dislocations show a decrease in image width for increasing order of reflection (i.e. increasing $\bar{g}\cdot\bar{b}$), thus enabling improved resolution of narrow dislocation dissociations and closely spaced dipoles or superdislocations. Experimental results have confirmed these predictions (e.g. refs. 2, 3). The technique is to orient the crystal to excite ng usually with $s > 0$, where n is the n^{th} order of the first reflection g_1. (see Fig. 8(b) Part 2 of my later Chap).

Dislocation image characteristics under systematic diffracting conditions have also been found useful for determining the magnitude of the product $g_1 b$ where g_1 is the first order reflection of the systematic set and thus can be of tremendous help when it is necessary

*Systematic orientation means a reciprocal lattice row along ng is excited; simultaneous orientation means several different rows are excited.

to choose between a number of different possibilities, and for examining more complex crystals. Examples of such application will be given in a later chapter, but here we indicate comparison between a known case and theory. In the fcc system, for an undissociated dislocation with Burgers vector of the type a/2 ⟨110⟩, when a 220 reflection is used the only three possibilities are $g_1 \cdot b$ equal to 0, 1, or 2. Figure 18 shows the image of a screw dislocation in Al compared to the image profile and multiple beam bright-field profiles obtained by computer methods for the possibilities $g_1 \cdot b = 1$ and 2. Comparing the trace of the image with the theoretical profiles it is clear that there is very good correspondence for the width of the central minima and the positions of all extrema for the $g_1 \cdot b = 2$ case. Variations in relative intensities in the experimental image are most likely due to thickness variations and discrepancies in dislocation depth.

(b) Planar Defects

The 12-beam systematic calculations for pure phase contrast (i.e., change in $\alpha = 2\pi \bar{g} \cdot \bar{R}$ with no changes in s, or g across the fault) indicate a surprising result (35). Bright field images were predicted to be contrasty or not depending on the sign of the phase change across the boundary (Fig. 19a, b). The effect is predicted at all voltages where strong systematic interactions occur. Although this general result has been confirmed for coherent thin hcp plates (equivalent to stacking faults $\alpha = \pm 2\pi/3$) in Al (Fig. 19(c-f) and for faults in silicon there are discrepancies in the details such as the thickness dependence of the intensity (2). Thus the potential applications of this

effect for determining the extrinsic or intrinsic nature of faults merely by inspection of bright field images must await further refinements of the theory. Attempts along these lines are in progress (34, 36).

ACKNOWLEDGEMENTS

These two chapters are abstracted from a book on electron microscopy in preparation by Dr. W. L. Bell and myself.

Most of the illustrations used are taken from our own research programs and I acknowledge continued financial support of the United States Atomic Energy Commission through the Inorganic Materials Research Division of the Lawrence Berkeley Laboratory. I am grateful to several past and present members of my group and to Dr. V. A. Phillips for permission to use unpublished results. These are indicated in the pertinent figure captions.

References Chapter II

1. D. J. H. Cockayne, Z. Für Naturf. 27, 452 (1972).

2. W. L. Bell and G. Thomas, 27th Conference Electron Microscope Society of America (Claitors Publishers) 1969, p. 156.

3. M. J. Goringe, E. A. Hewatt, C. J. Humphries and G. Thomas, Proc. 5th European Electron Microscopy Congress, Inst. Phys. London 1972, p. 538.

4. Electron Microscopy and Structure of Materials (Ed. G. Thomas) Univ. of Calif. Press (1972) Chapters 1-3.

5. Modern Diffraction and Imaging Techniques in Materials Science (Eds. S. Amelinckx et.al.) N. Holland (1970).

6. Electron Microscopy in Materials Science (Ed. U. Valré) Academic Press 1972.

7. R. Siems, P. Delavignette and S. Amelinckx, Phys. Stat. Sol., 2 (1), 421, (1962). See also ref. 2, p. 158

8. W. L. Bell and G. Thomas, Phys. Stat. Sol., 12, 843, (1965).

9. M. von Heimendahl, Micron (1973) in press, LBL report 1186.

10. P. R. Okamoto, E. Levine and G. Thomas, J. Appl. Physics 38, 289 (1967).

11. P. R. Okamoto and G. Thomas, Phys. Stat. Soc., 25, 81 (1968).

12. P. B. Hirsch et.al., Electron Microscopy of Thin Crystals Butterworths 1965

13. E. Levine, W. L. Bell and G. Thomas, J. Appl. Phys. 37, 2141 (1966)

14. P. R. Okamoto and G. Thomas, Acta Met. 15, 1325 (1967).

15. L. M. Clarebrough, Austr. J. Physics 24, 79 (1971).

16. A. K. Head, Austr. J. Physics 20, 557 (1967).

17. W. L. Bell, W. R. Roser and G. Thomas, Acta Met. 12, 1247 (1964).

18. W. L. Bell and G. Thomas, Phil. Mag. 13, 395 (1966).

19. G. Thomas and W. L. Bell, Lattice Defects and their Interactions (Ed. R. Hasiguti) Gordon & Breach N.Y. (1967) p. 477.

20. M. J. Whelan and P. B. Hirsch, Phil. Mag. 2, 1121 (1957).

21. H. Hashimoto, A. Howie and M. J. Whelan, Proc. Roy Soc. A269 80 (1962).

22. R. Gevers, A. Art and S. Amelinckx, Phys. Stat. Sol. 3, 1563 (1963).

23. S. Amelinckx, ref. 5, p. 257.

24. M. J. Marcinkowski, Electron Microscopy and Structure of Materials (Ed. G. Thomas) Univ. of Calif. Press 1972, p. 382.

25. Surface Science 31, 1972 (Publication of papers given at an International Conference on Interfaces, IBM New York 1971).

26. G. Thomas ref. 5, p. 131.

27. P. J. Fillingham, H. J. Leamy and L. E. Tanner, ref. 4 p. 163.

28. V. A. Phillips and L. E. Tanner, Acta Met. in press (1973).

29. V. A. Phillips, ibid.

30. M. Wilkens, ref. 5, p. 233.

31. D. M. Maher and R. E. Villagrana, private communication.

32. W. L. Bell, Proc. 29th EMSA Conference Claitors Publishers (1969) p. 156.

33. L. C. de Jonghe and W. L. Bell, 7th Int. Congress Electron Microscopy, Grenoble, (1970) 2 337.

34. R. Osiecki, L. C. de Jonghe, W. L. Bell and G. Thomas, to be published.

35. W. L. Bell, 7th Int. Congress Electron Microscopy, Grenoble (1970) 2, 81.

36. L. Chen, Ph.D. thesis in progress (Univ. of Calif., Berkeley).

CHAPTER 2 FIGURE CAPTIONS

Fig. 1. a) Bright field and b, c, d, weak beam dark field images of interphase boundary dislocations in over-aged Cu-Mn-Al alloy showing images ~ 20Å wide. These are high resolution, kinematical images ($s \gg 0$) formed in -g with [$ng\ s > 0$] excited where n = 3 or larger (See Fig. 2). D. Cockayne and G. Thomas (unpublished).

Fig. 2. As Fig. 1 (different foil) bright field image with $g(s > 0)$ excited {courtesy Surface Science, Livak, Bouchard and Thomas ref 25}. Notice the image width of these dislocations is much greater than in Fig. 1. Both Figs. 1, 2 show that the dislocations are pure edge (undissociated) with $\vec{b}$ in ⟨100⟩ directions. The diffraction pattern (d) shows the alloy is ordered (L21 structure).

Fig. 3. Contrast from dislocation loops around θ' plates in aged Al-4%Cu alloy. The loops lie in {100} and are pure edge with $\vec{b}$ in ⟨100⟩. For plates normal to the beam $\bar{g}\cdot\bar{b} = 0$ and $\bar{g}\cdot\bar{R}_n$ is radial and zero along directions normal to $\vec{g}$. This gives rise to "residual" arced contrast. The dislocations around 010 plates are invisible since $\bar{g}\cdot\bar{b}_{(010)} = 0$.

Fig. 4. 'Contrast from spherically symmetrical strain fields due to precipitation in Cu-Co alloy (Courtesy Ashby and Brown, Phil. Mag. 8, 1649 1963). Notice similarity to arc contrast in Fig. 3.

Fig. 5. Illustrating the use of the Kikuchi map for analysing the slip band structure in deformed Ag_2Al (ref 10 Courtesy J. Appl. Physics).

Fig. 6. Scheme showing that a dislocation locally tilts reflecting planes closer to or away from the Bragg condition on opposite sides of the extra half plane. (a) and (b) would be reversed if the dislocation was inverted (extra half plane down). The images are therefore to one side of the true position of the dislocation.

Fig. 7(a). Illustrating an application of Fig. 6 for distinguishing between dipoles and superdislocations; three different methods all involving tilting are shown (ref. 17, Courtesy Acta Met.) (b,c) Application of Fig. 7a to dislocations in austenitic stainless steel: B are dipoles, A are superdislocations indicating the alloy is ordered (ref. 17 Courtesy Acta Met).

Fig. 8. Scheme showing image behavior of large, perfect, dislocation loops in crystals when $\bar{g}$ or $\bar{s}$ changes sign (Courtesy Amer. Soc. Metals ref. Thin Films 1964, p. 227).

Fig. 9. Quenched aluminum containing perfect loops on {111}: loops B increase in size as the sign of $\vec{g}$ is changed from (a) to (b) [$s > 0$, as shown by the diffraction patterns] loops A go out of contrast in $g = \bar{2}\bar{2}0$ so $\vec{b} = a/2[1\bar{1}0]$. Notice that this $\vec{b}$ is normal to the [110] no contrast lines of the double-arc images of loops A in (a). (ref. 18 Courtesy Phil. Mag.)

Fig. 10. Scheme predicting visibility of partial dislocations and associated stacking faults in fcc crystals.

Fig. 11. Partial dislocations and stacking faults in austenitic stainless steel (cf Fig. 10).

Fig. 12. Contrast experiments for faults in $TaC_{0.8}$ a, b, c bright field images showing the shear nature of the faults $\{\vec{b} = \langle 112 \rangle\}$. The faults do not completely vanish in (b-d), indicating local changes in composition (structure factor contrast). The dark field image in (d) shows that (111) and $(1\bar{1}\bar{1})$ are intrinsic and extrinsic respectively.

Fig. 13. Intensity distribution for $\alpha = \pm 2\pi/3$ contrast as predicted by two-beam dynamical theory with absorption.

Fig. 14. Scheme showing orientation of intrinsic (top row) and extrinsic (lower row) stacking faults with respect to $\vec{g}$ for determining fault character (See Table 4)(from ref. 22).

Fig. 15. Contrast from intrinsic faults in silicon; (a) bright field (b) dark field showing the predicted behavior of Fig. 13; c, d shows the asymmetry properties of dark field for $s \neq 0$ enabling the first, or last, fringe to be immediately identified. (ref. 8 Courtesy Phys. Stat. Sol.)

Fig. 16. Scheme showing contrast expected from overlapping faults in fcc crystals with $\alpha = \pm 2\pi/3$ Band W are dark and light fringes respectively.

Fig. 17. Showing three contrast mechanisms for imaging small coherent plates of G. P. zones or θ" in Al-Cu alloys a) bright field diffraction contrast b) structure factor contrast dark field image of the streak in c), (d) Two beam tilted (002) lattice images of G. P. zones. a, b, c Al-4%Cu - 0.5%Sn ref 26 Courtesy N-Holland d) Al-3%Cu courtesy V. A. Phillips and Acta Met (in press).

Fig. 18. Comparison between observed and calculated image contrast for a/2 ⟨110⟩ screw dislocation in aluminum. The magnitude of the Burgers vector is found from the fringe spacings, not from their intensities. $\bar{g}_1 \cdot \bar{b} = 2$ in this case 650 kV systematic 12 beam case (ref. 34).

Fig. 19. a, b 12 beam systematic contrast calculation for stacking faults in fcc crystals upper curves bright field, lower curves dark field. Notice stronger bright field fringe contrast for $\bar{g} \cdot \bar{R} = -\frac{1}{3}$ than $+\frac{1}{3}$. (430 kV Al-1%Ag) c, d $\pm g$ bright field images of thin hcp platelets in Al-1%Ag alloy (430 kV) e.f. corresponding dark field images Courtesy W. L. Bell.

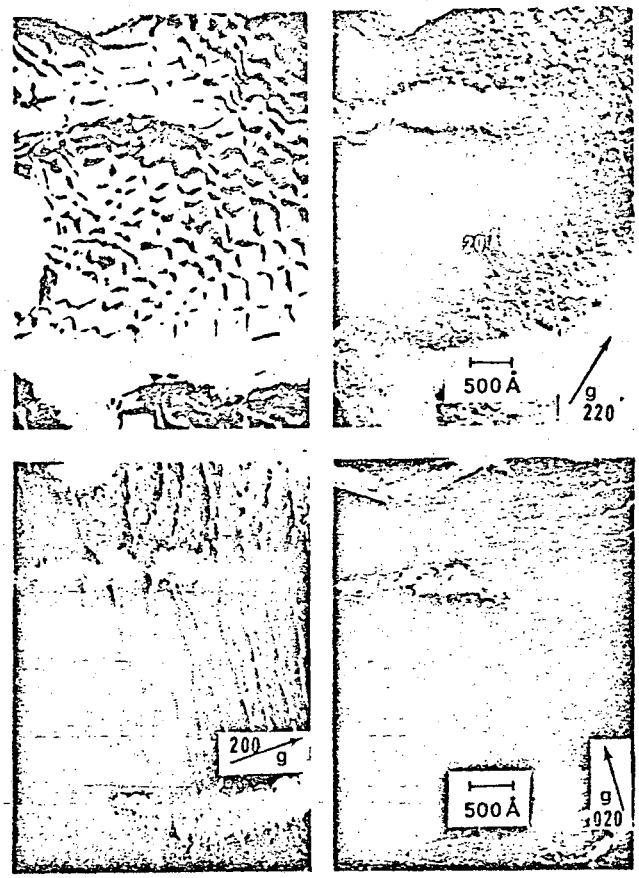

XBB 7211 5715

Fig. 1

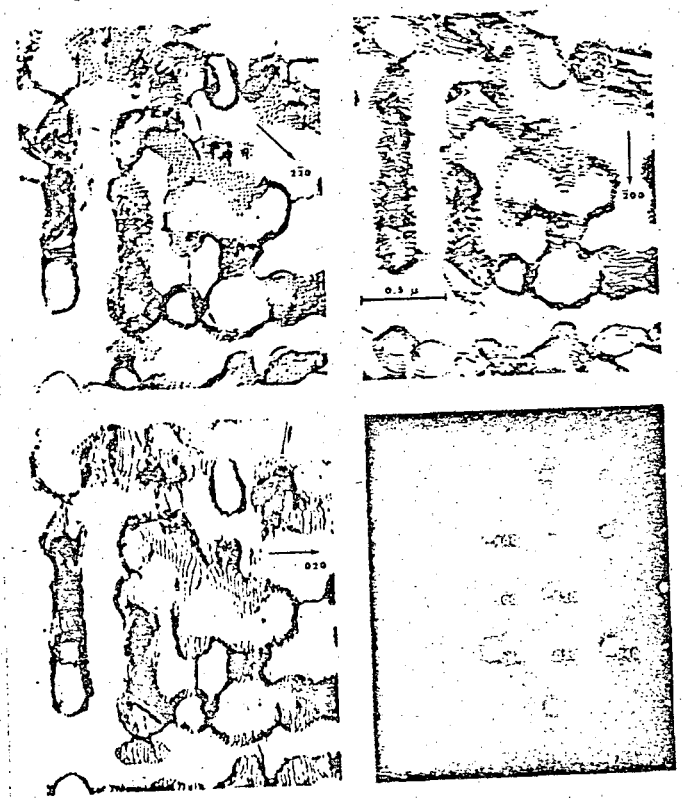

XBB 718 3544

Fig. 2

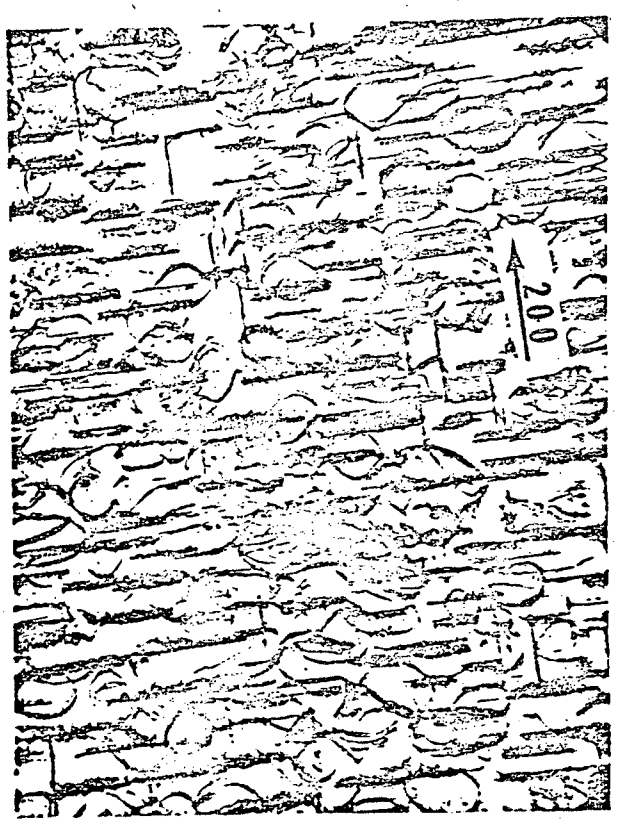

XBB 695 3498

Fig. 3

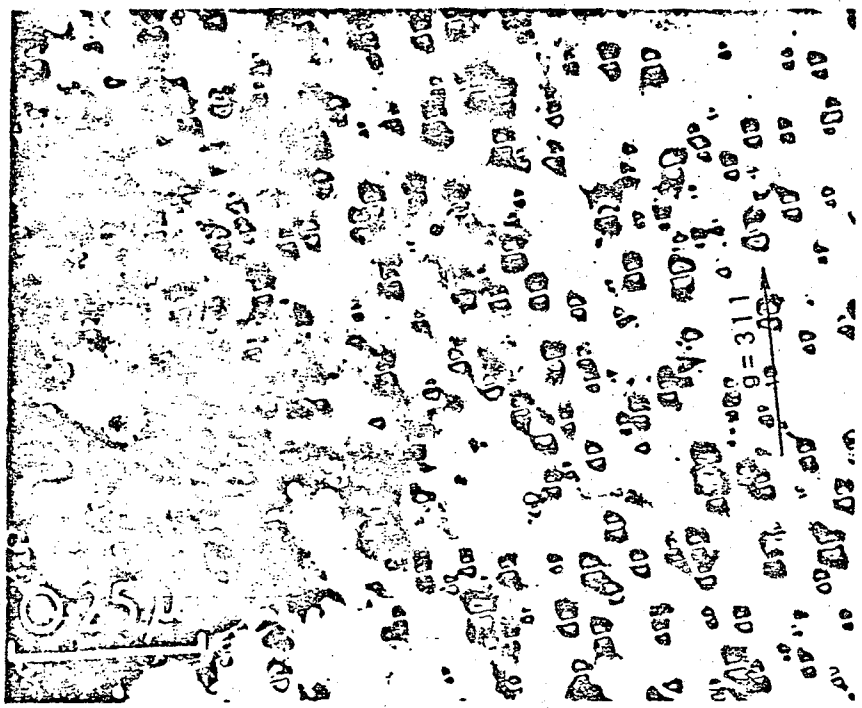

ZN 4016

Fig. 4

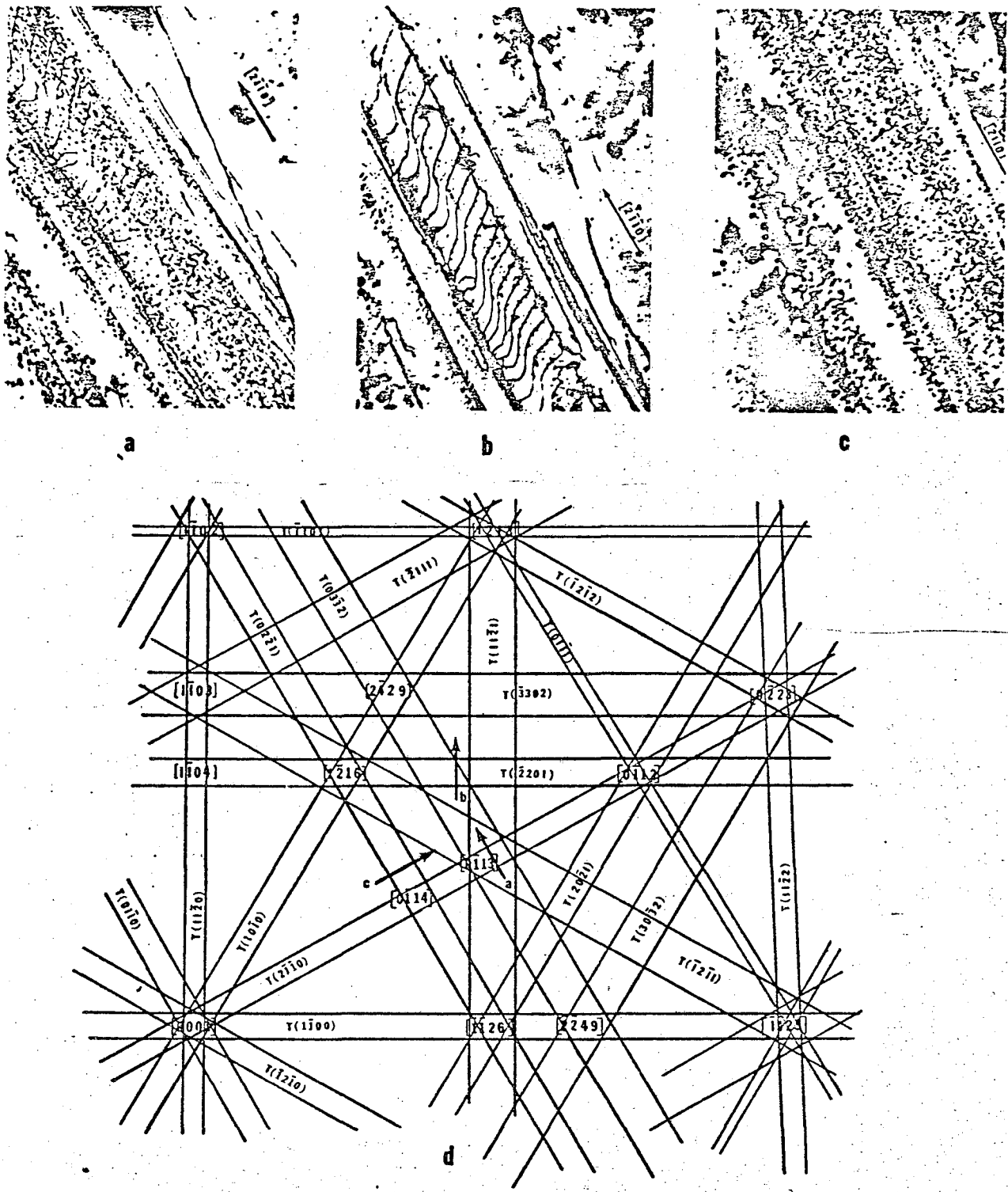
a
b
c
d
[2110]
[2110]
[2110]
[1103]
[2429]
T(3302)
[0122]
[1104]
[216]
T(2201)
[011]
[114]
[1123]
[1126]
[2249]
[1122]
[001]
T(1100)
T(1120)
T(1010)
T(2110)
T(1210)
T(0112)
T(0221)
T(2111)
T(1121)
T(1011)
T(2021)
T(3032)
T(1122)
T(2111)

IM 2097

Fig. 5

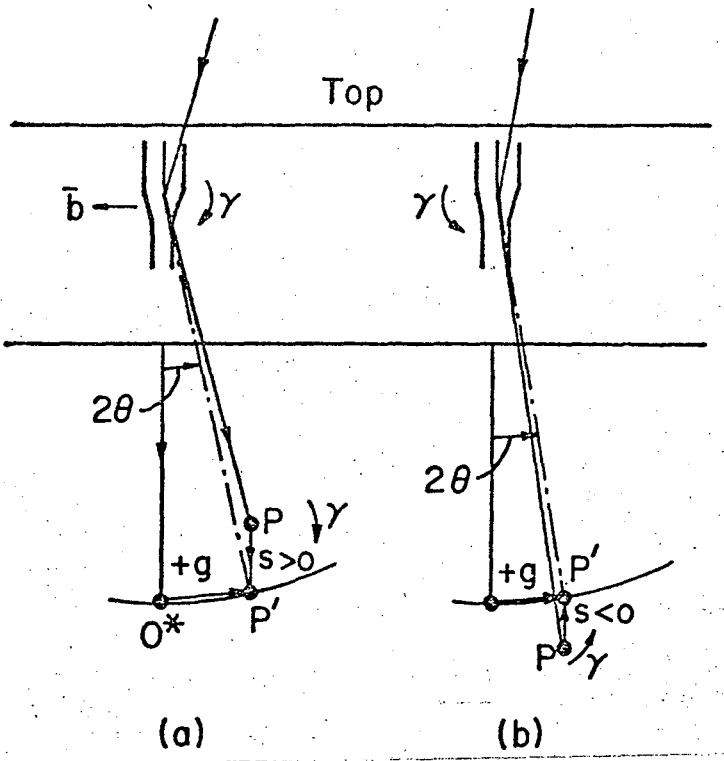

MU-32262

Fig. 6

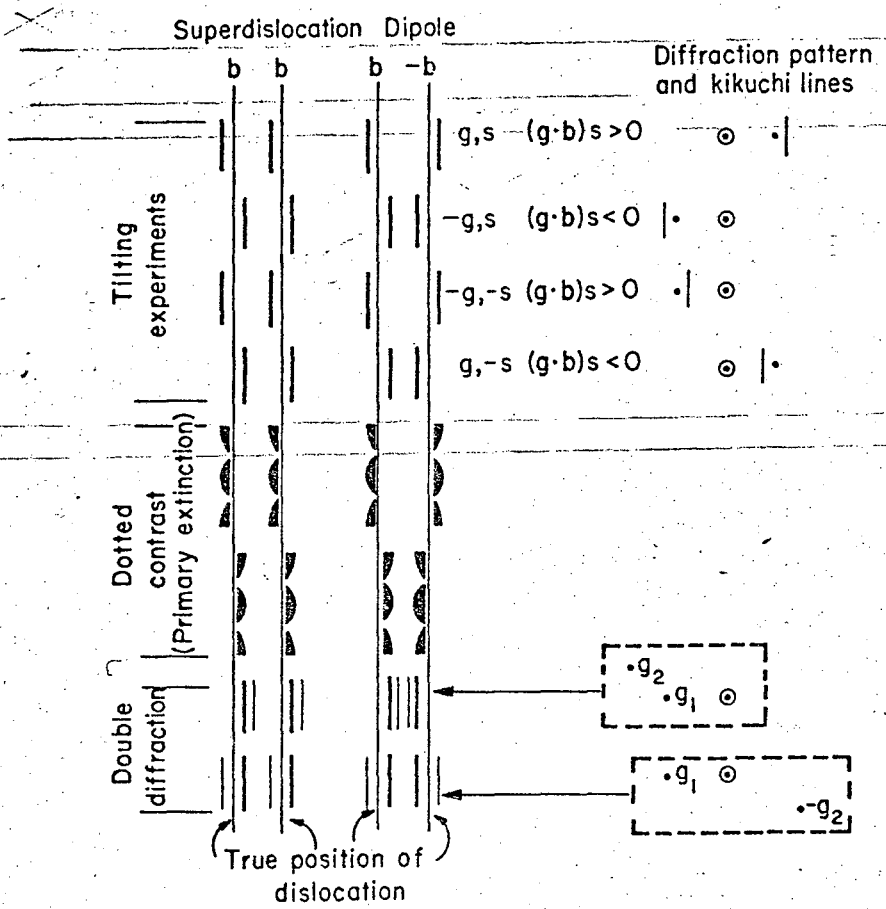

Fig. 7a

MU-33340

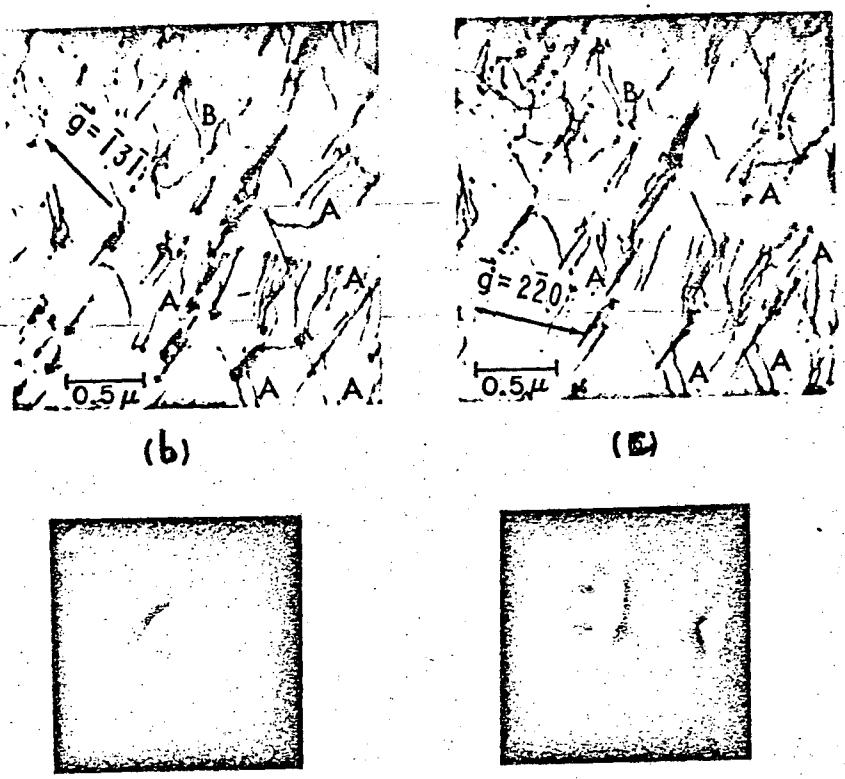

Fig. 7

IM 970

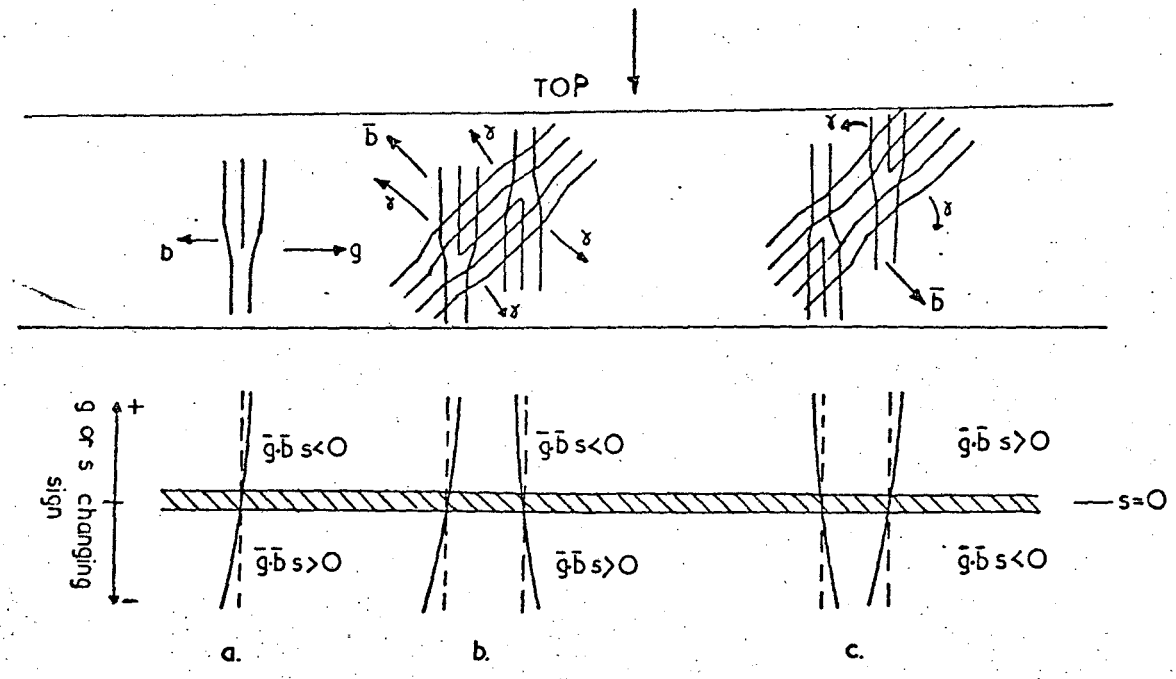

MU-32181

Fig. 8

IM 1745

Fig. 9

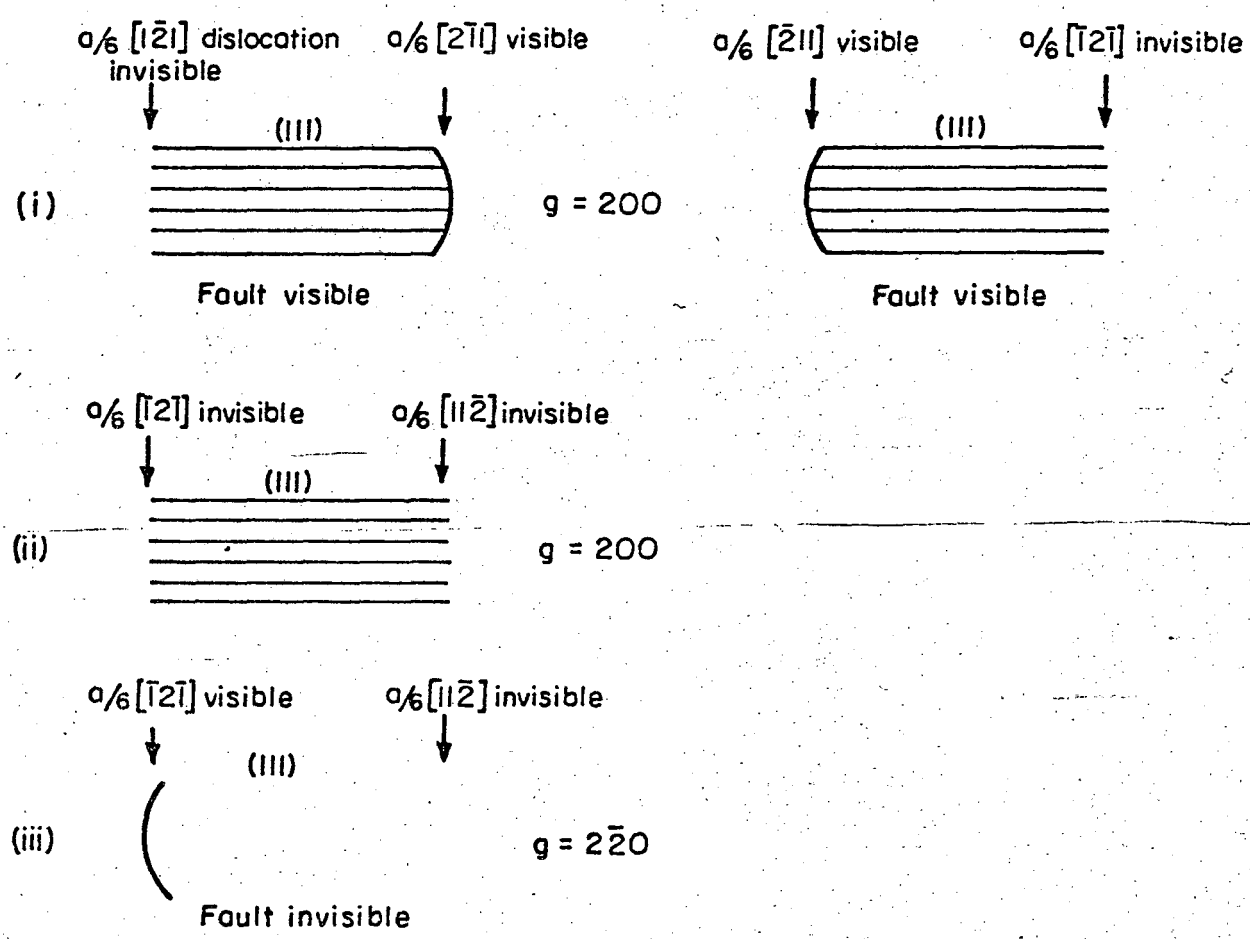

XBL 731-5665

Fig. 10

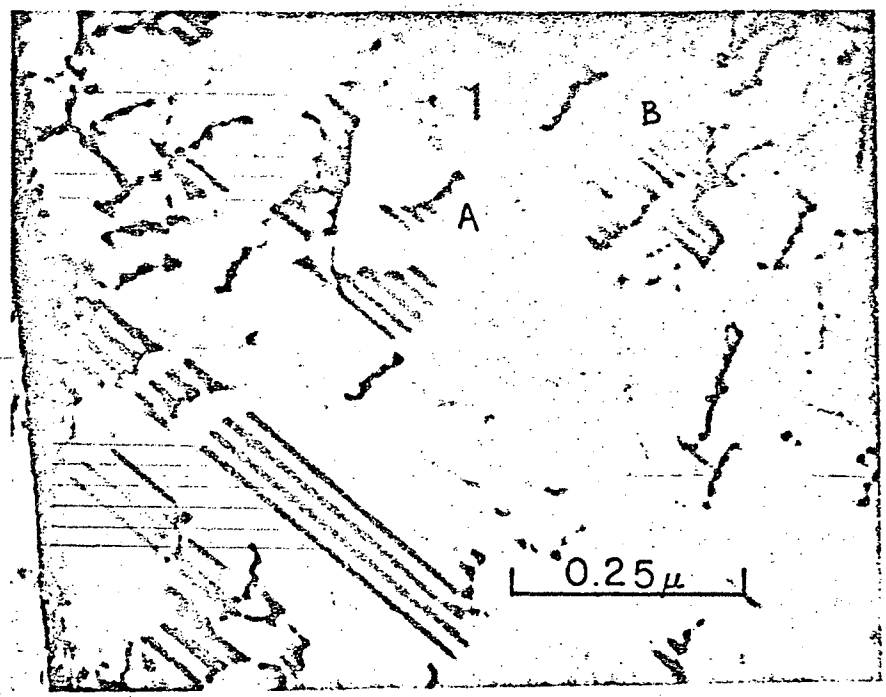

IM 814

Fig. 11

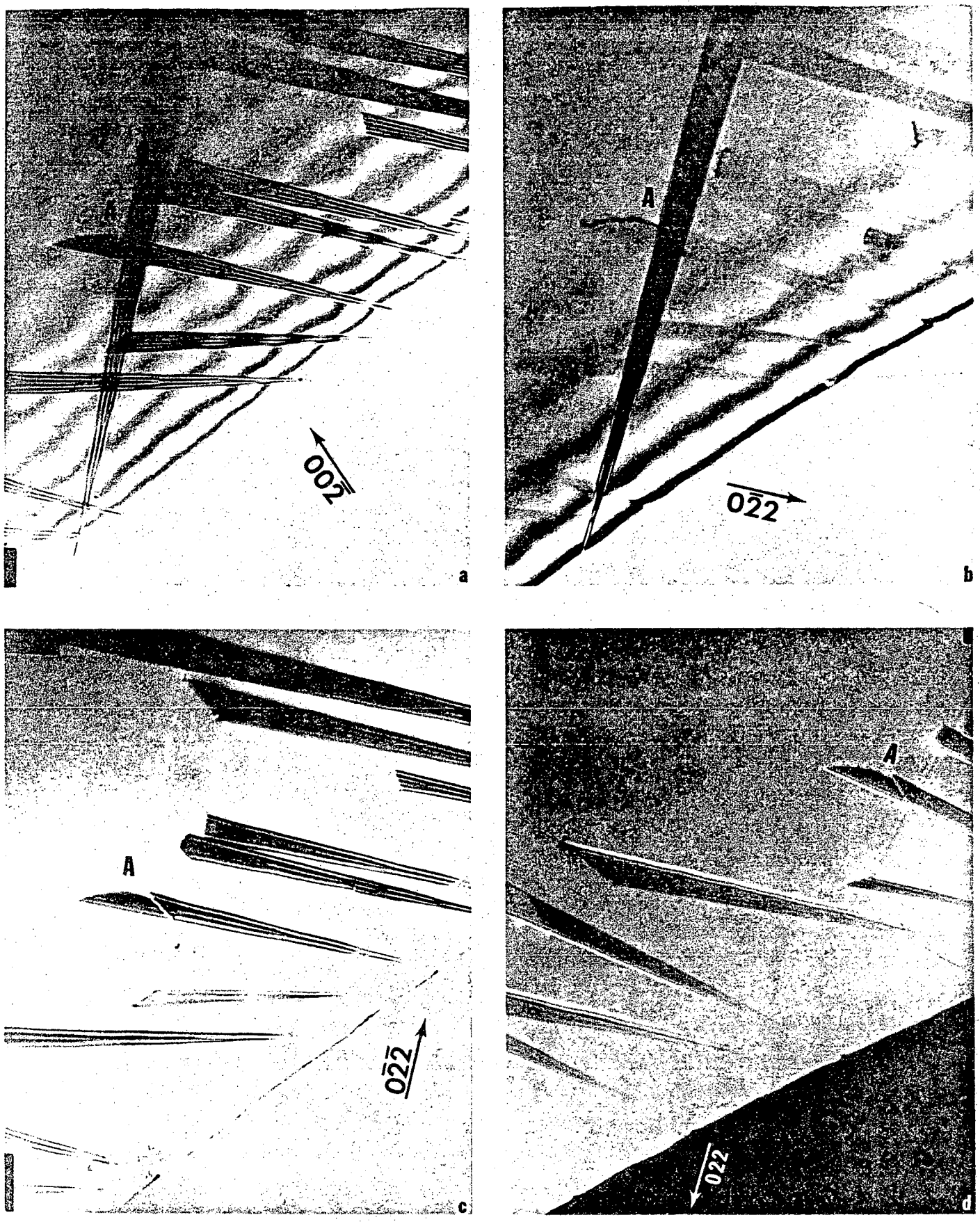

XBB 737-4136

Fig. 12

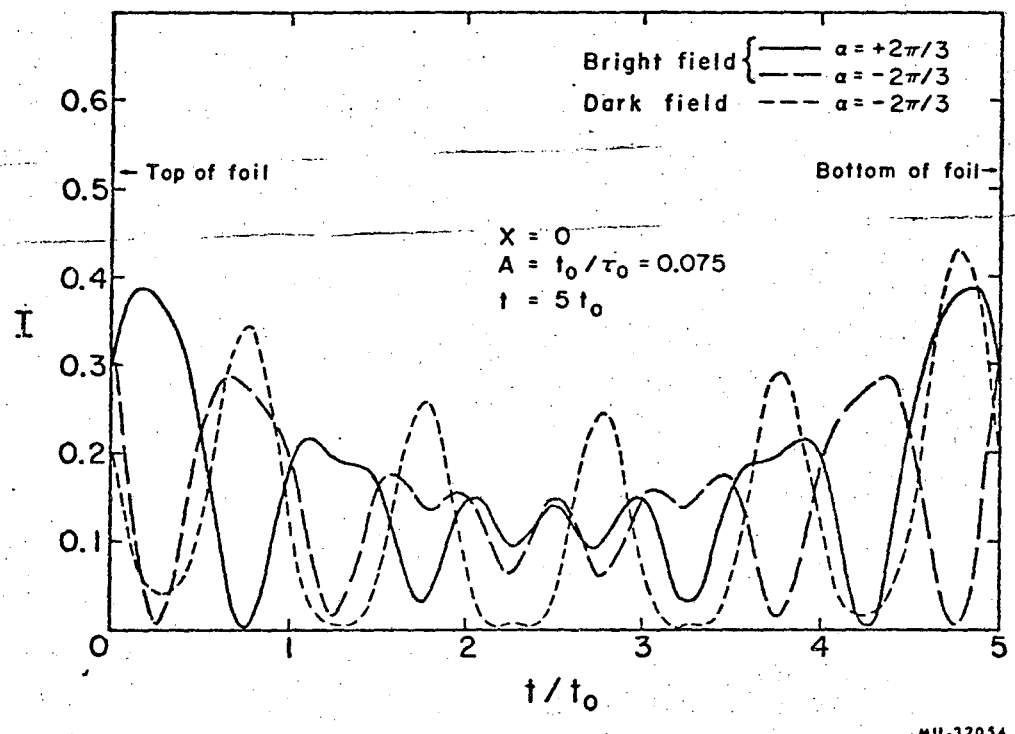
Bright field { α = +2π/3
α = -2π/3
Dark field α = -2π/3
Top of foil
Bottom of foil
X = 0
A = t0 / τ0 = 0.075
t = 5 t0
I
0.6
0.5
0.4
0.3
0.2
0.1
0
1
2
3
4
5
t / t0
MU-32054

Fig. 13

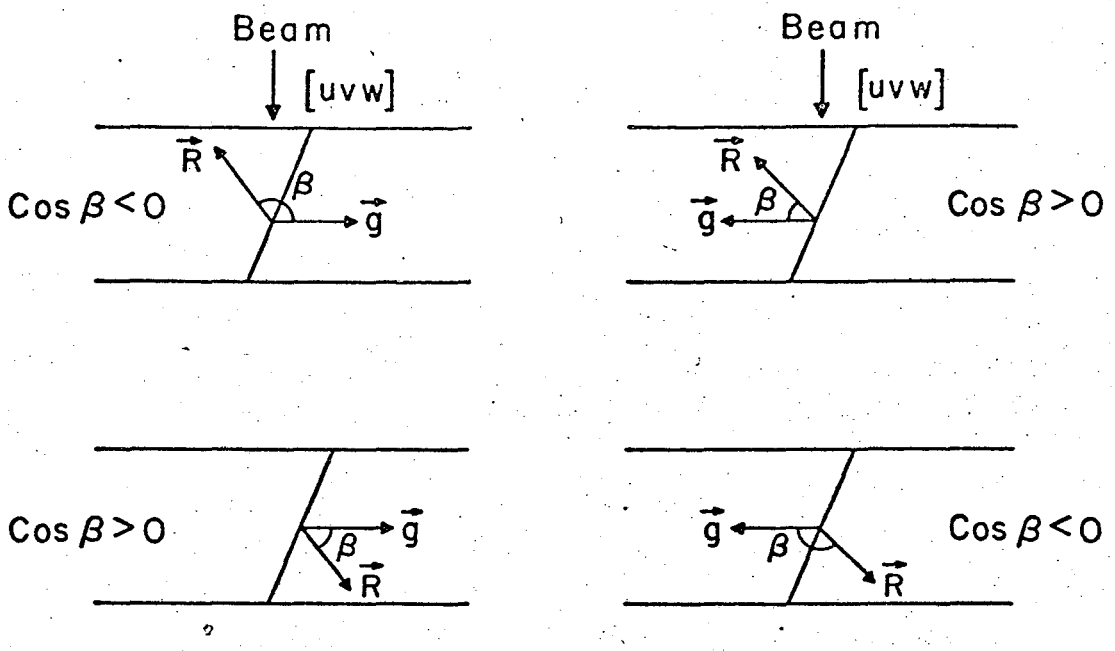

Fig. 14

MU-32113

ZN 4013

Fig. 15

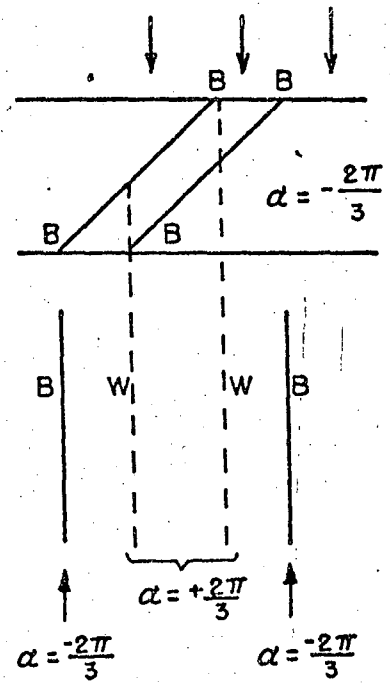

Two intrinsic or extrinsic

(a)

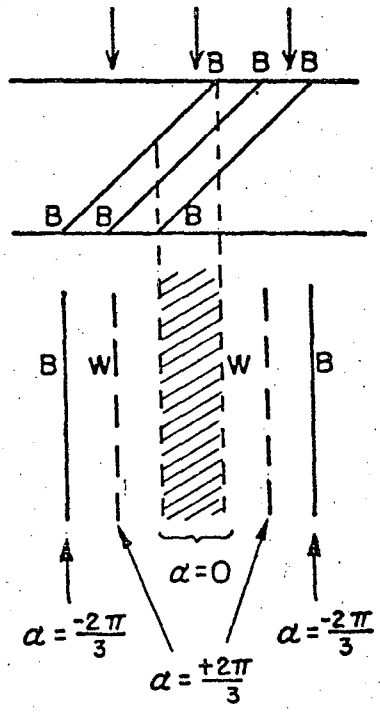

All intrinsic or extrinsic

(b)

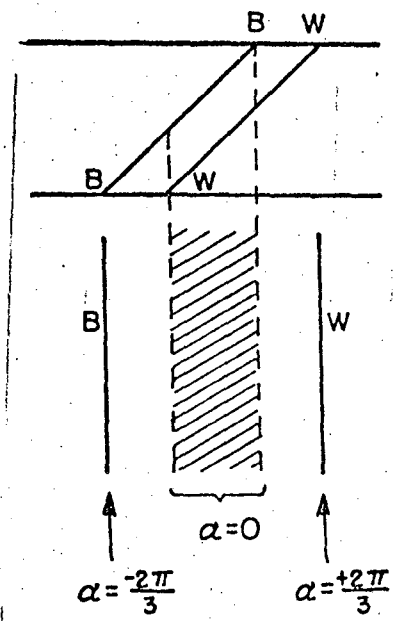

One intrinsic, one extrinsic

(c)

XBL 731-5664

Fig. 16

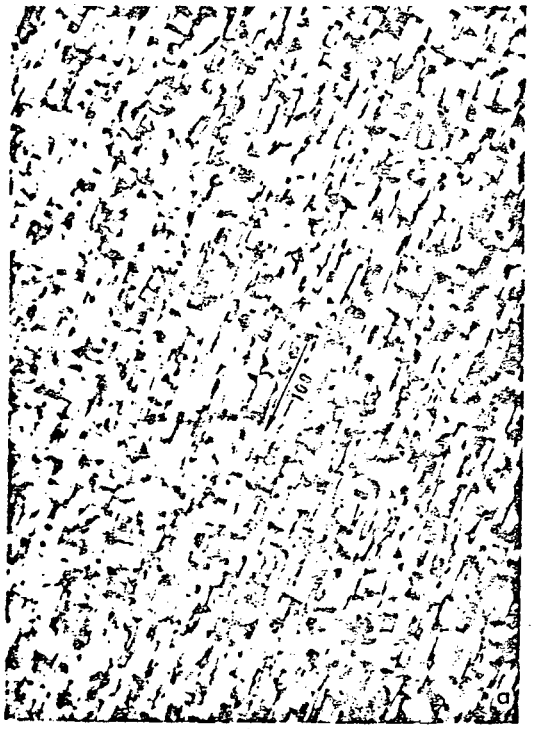

a

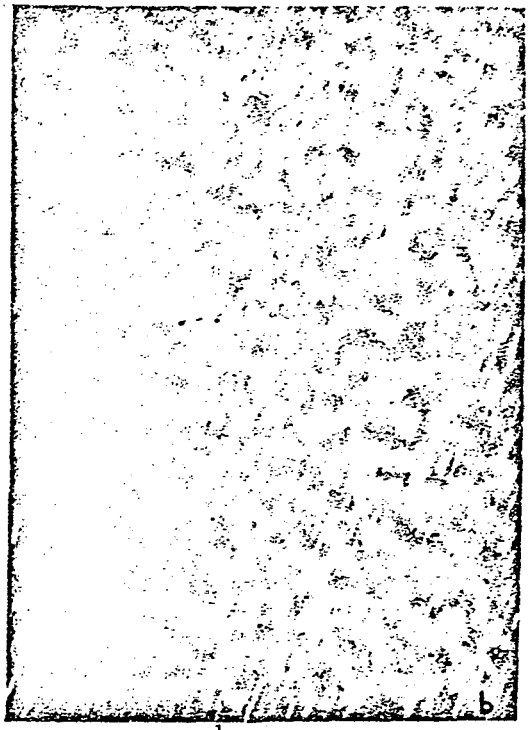

b

XBB 699 6018

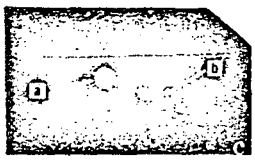

c

0.2 μ

Fig. 17

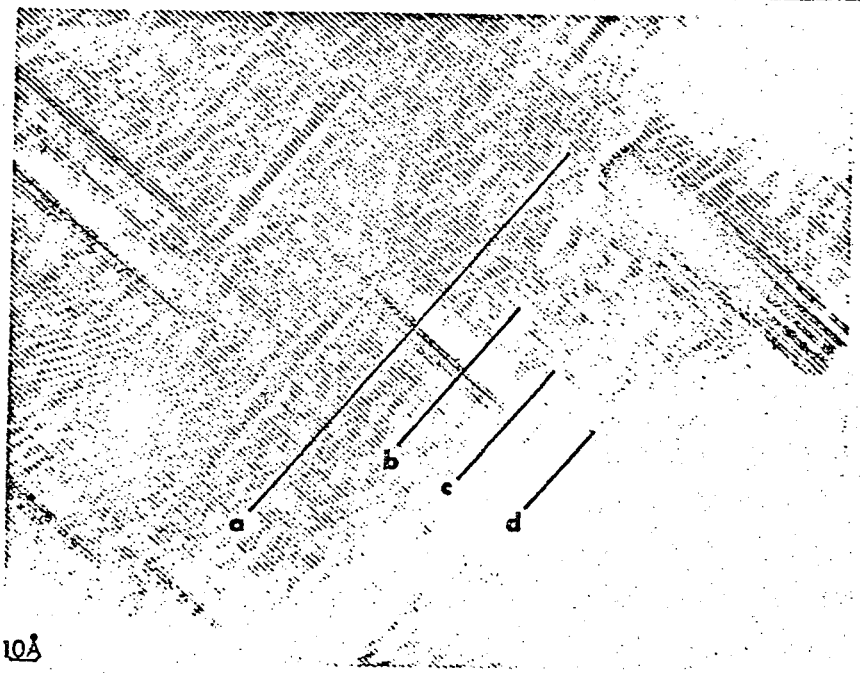

10Å

XBB 731 488

Fig. 17d

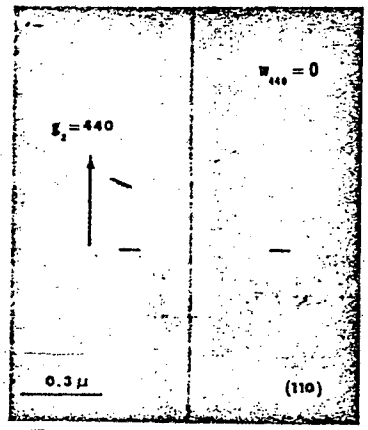

Al.

FOIL THICKNESS :

8300 Å

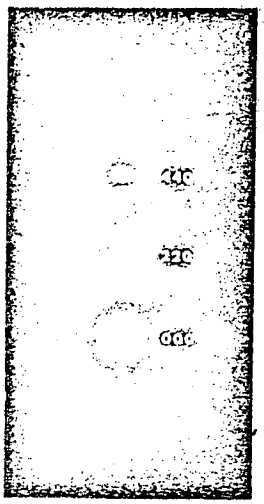

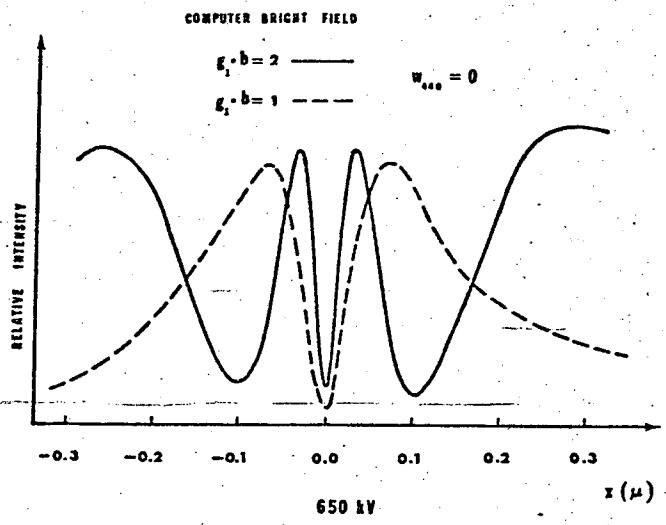

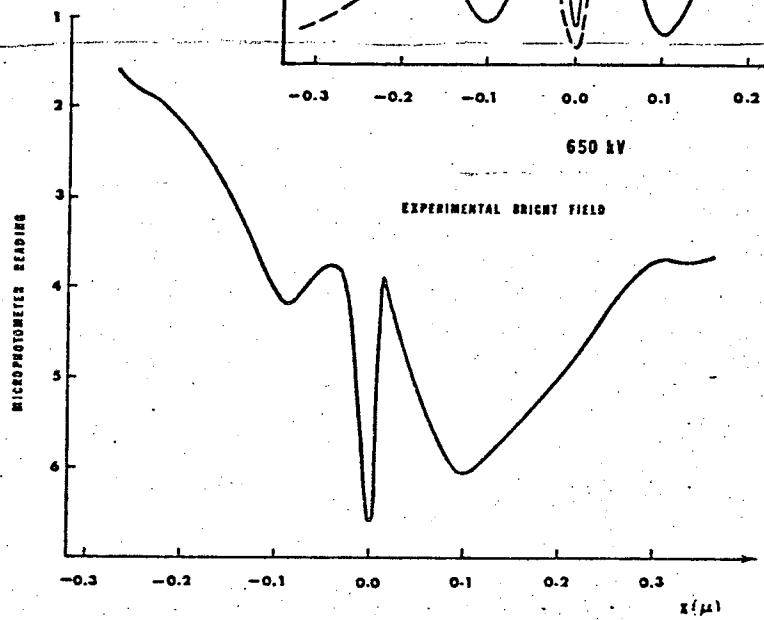

XBB 7011 5224

Fig. 18

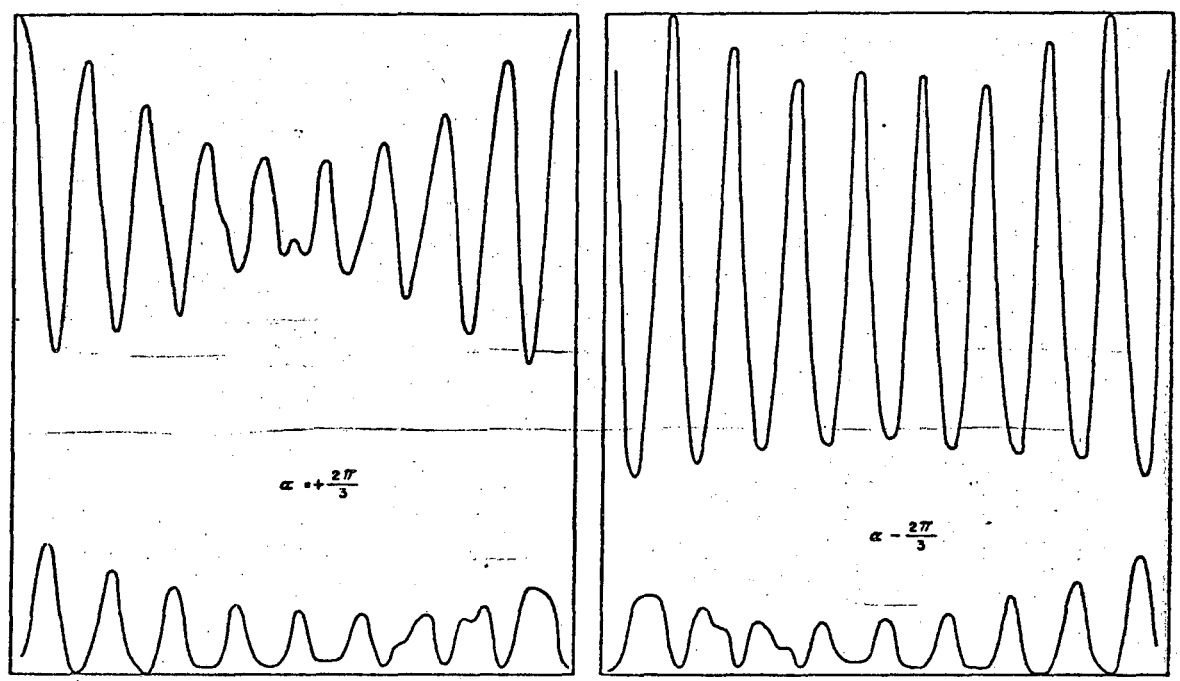

STACKING FAULT PROFILES – ALUMINUM (000), (222), 430Kv.

XBL 702-409

Fig. 19

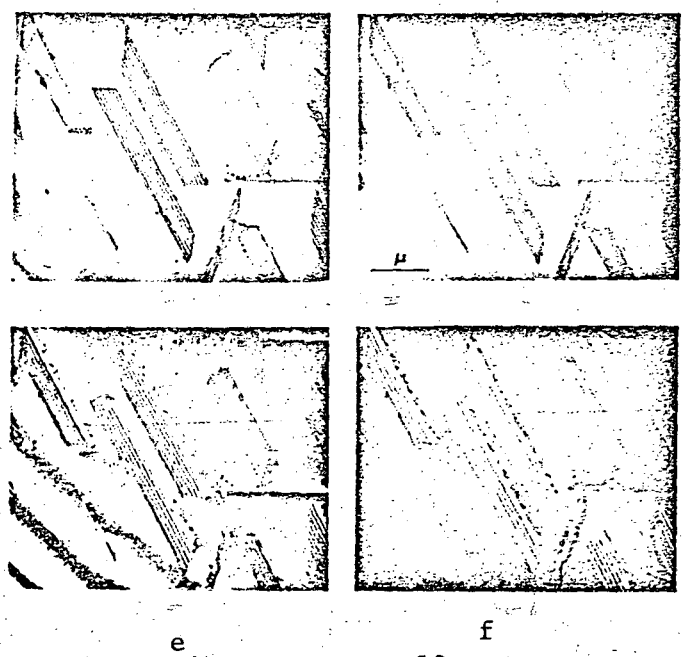

Fig. 19

TECHNICAL INFORMATION DIVISION
LAWRENCE BERKELEY LABORATORY
UNIVERSITY OF CALIFORNIA
BERKELEY, CALIFORNIA 94720